Journal of Environmental Chemical Engineering xxx (xxxx) 113026

Contents lists available at ScienceDirect

Journal of Environmental Chemical Engineering

journal homepage: www.elsevier.com/locate/jece

Sulfamerazine degradation employing a novel Z-scheme $TiO_2/KNbO_3$/g-C_3N_4 photocatalyst under artificial sunlight: Insights on degradation mechanism and toxicity

Nicolas Perciani de Moraes [a,*], Tiago Moreira Bastos Campos [b], Gilmar Patrocínio Thim [b], Yu Lianqing [c], Robson da Silva Rocha [d], Renata Colombo [e], Liana Alvares Rodrigues [d,*], Marcos Roberto de Vasconcelos Lanza [a,*]

[a] São Carlos Institute of Chemistry, University of São Paulo, Av. Trab. São Carlense, 400 - Parque Arnold Schimidt, São Carlos, SP 13566-590, Brazil
[b] Aeronautics Institute of Technology - ITA/CTA, Praça Mal. Eduardo Gomes 50, São José dos Campos, São Paulo CEP 12228-900, Brazil
[c] School of Materials Science and Engineering, China University of Petroleum, QingDao 266580, China
[d] Lorena School of Engineering, EEL/USP, Estrada Municipal do Campinho S/N, Lorena, São Paulo CEP 12602-810, Brazil
[e] School of Arts, Sciences and Humanities, University of São Paulo, São Paulo, São Paulo 03828-000, Brazil

ARTICLE INFO

Keywords:
Titanium oxide
potassium niobate
graphitic carbon nitride
photocatalysis
Z-scheme heterojunction
sulfamerazine

ABSTRACT

The development of a novel $TiO_2/KNbO_3$/g-C_3N_4 photocatalyst for the degradation of sulfamerazine under artificial sunlight was investigated in this study, aiming to obtain a highly effective material through the formation of Z-scheme heterojunctions between the proposed semiconductors. The characterizations confirmed the formation of the intended heterojunctions in the ternary composite photocatalyst, as the presence of TiO_2, $KNbO_3$, and g-C_3N_4 was successfully verified. Furthermore, the coupling between the semiconductors in the form of the ternary photocatalyst led to structural, morphological, and optical modifications of the TiO_2 base matrix, such as a higher specific surface area and larger visible light absorption. The optimized ternary material (TiO_2-5% $KNbO_3$-0.25% g-C_3N_4) exhibited the highest reaction degradation capacity for the sulfamerazine (SFMZ) in both solar (86.5% degradation) and visible light (60% degradation) tests, confirming a significant enhancement over the pure TiO_2, which achieved 48% degradation under solar light and 10% degradation under visible light. This result was mainly attributed to the formation of Z-scheme heterojunctions between the semiconductors, which enhanced the charge-transport efficiency during photonic excitation. Lastly, the degradation pathway proposed using mass spectroscopy analysis indicated the formation of mainly less toxic intermediates, as estimated through quantitative structure-activity relationship (QSAR) predictions.

1. Introduction

Nowadays, the release of antibiotics into the environment poses a significant hazard with extensive repercussions, as their widespread use has led to the contamination of water bodies through various pathways, notably via wastewater discharge and agricultural runoff [1]. Among the most concerning risks associated with this kind of environmental pollution is the rise of antibiotic-resistant bacteria, as prolonged exposure to low doses of antibiotics in the environment can select genetically resistant bacteria, potentially rendering these crucial drugs ineffective [2,3]. In this context, the uncontrolled development of antibiotic-resistant organisms can pose a significant challenge to global health, as this phenomenon leads to longer hospitalizations, higher medical costs, and increased mortality rates [4]. Consequently, immediate action must be taken to address the risks posed by uncontrolled antibiotic release into the environment, including effective and sustainable solutions for wastewater treatment.

Considering antibiotics commonly released in effluents, the sulfamerazine (SFMZ) compound from the sulfonamide class can be isolated as a molecule of interest. This antibiotic is used to treat a variety of bacterial infections in humans and is commonly added to animal feed in the livestock industry for the prevention and treatment of bacterial infections [5,6]. However, once ingested, this antibiotic is incompletely metabolized, as nearly 75% of the administered dose is excreted in its original form [7]. Thus, SFMZ can be detected at concentrations between ng L^{-1} and μg L^{-1} in effluents from the livestock industry and surrounding water bodies, with this accumulation being enhanced by the high resistance of this antibiotic to natural degradation processes [7].

* Corresponding authors.
E-mail addresses: nicolas.perciani@usp.br (N.P. de Moraes), liana.r@usp.br (L.A. Rodrigues), marcoslanza@usp.br (M.R. de Vasconcelos Lanza).

https://doi.org/10.1016/j.jece.2024.113026
Received 16 January 2024; Received in revised form 5 April 2024; Accepted 8 May 2024
2213-3437/© 20XX

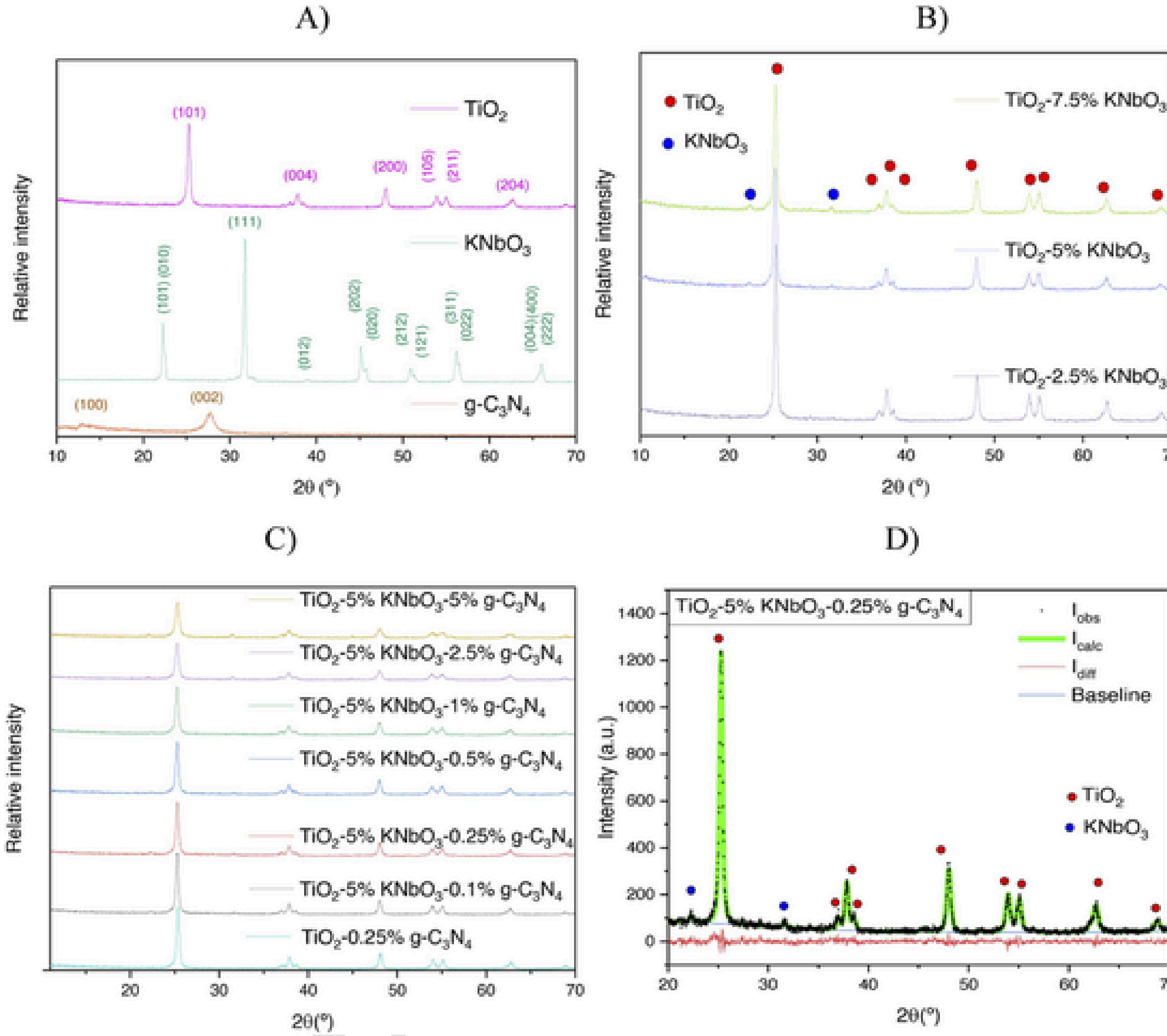

Fig. 1. A) X-ray diffractograms for the pure semiconductors (TiO_2, $KNbO_3$ and $g-C_3N_4$); B) X-ray diffractograms for the binary photocatalysts (TiO_2-w% $KNbO_3$); C) X-ray diffractograms for the ternary photocatalysts (TiO_2-5% $KNbO_3$-y% $g-C_3N_4$) and binary TiO_2-0.25% $g-C_3N_4$; D) Rietveld refinement results for the TiO_2-5% $KNbO_3$-0.25% $g-C_3N_4$ sample.

Table 1 –
Rietveld refinement applied to the diffractograms of the developed materials.

Material	TiO_2 (tetragonal)				$KNbO_3$ (orthorhombic)				χ^2
	a (nm)	c (nm)	L_c (nm)	w%	a (nm)	b (nm)	c (nm)	w%	
TiO_2	0.379	0.951	22.19	100	-	-	-	-	1.05
TiO_2-2.5% $KNbO_3$	0.379	0.951	22.55	99.2	0.397	0.564	0.566	0.8	1.12
TiO_2-5% $KNbO_3$	0.379	0.951	22.05	98.5	0.398	0.564	0.566	1.5	1.18
TiO_2-7.5% $KNbO_3$	0.379	0.951	22.62	97.6	0.397	0.567	0.566	2.4	1.34
TiO_2-0.25% $g-C_3N_4$	0.379	0.951	22.34	100	-	-	-	-	1.18
TiO_2-5% $KNbO_3$-0.1% $g-C_3N_4$	0.379	0.951	22.54	98.7	0.397	0.564	0.565	1.3	1.30
TiO_2-5% $KNbO_3$-0.25% $g-C_3N_4$	0.379	0.951	22.30	98.4	0.398	0.565	0.566	1.6	1.10
TiO_2-5% $KNbO_3$-0.5% $g-C_3N_4$	0.379	0.951	22.19	98.6	0.396	0.568	0.567	1.4	1.08
TiO_2-5% $KNbO_3$-1% $g-C_3N_4$	0.379	0.951	21.13	98.5	0.396	0.564	0.566	1.5	1.30
TiO_2-5% $KNbO_3$-2.5% $g-C_3N_4$	0.379	0.951	18.59	98.2	0.397	0.565	0.566	1.8	1.41
TiO_2-5% $KNbO_3$-5% $g-C_3N_4$	0.379	0.951	17.29	98.1	0.397	0.564	0.566	1.9	1.17

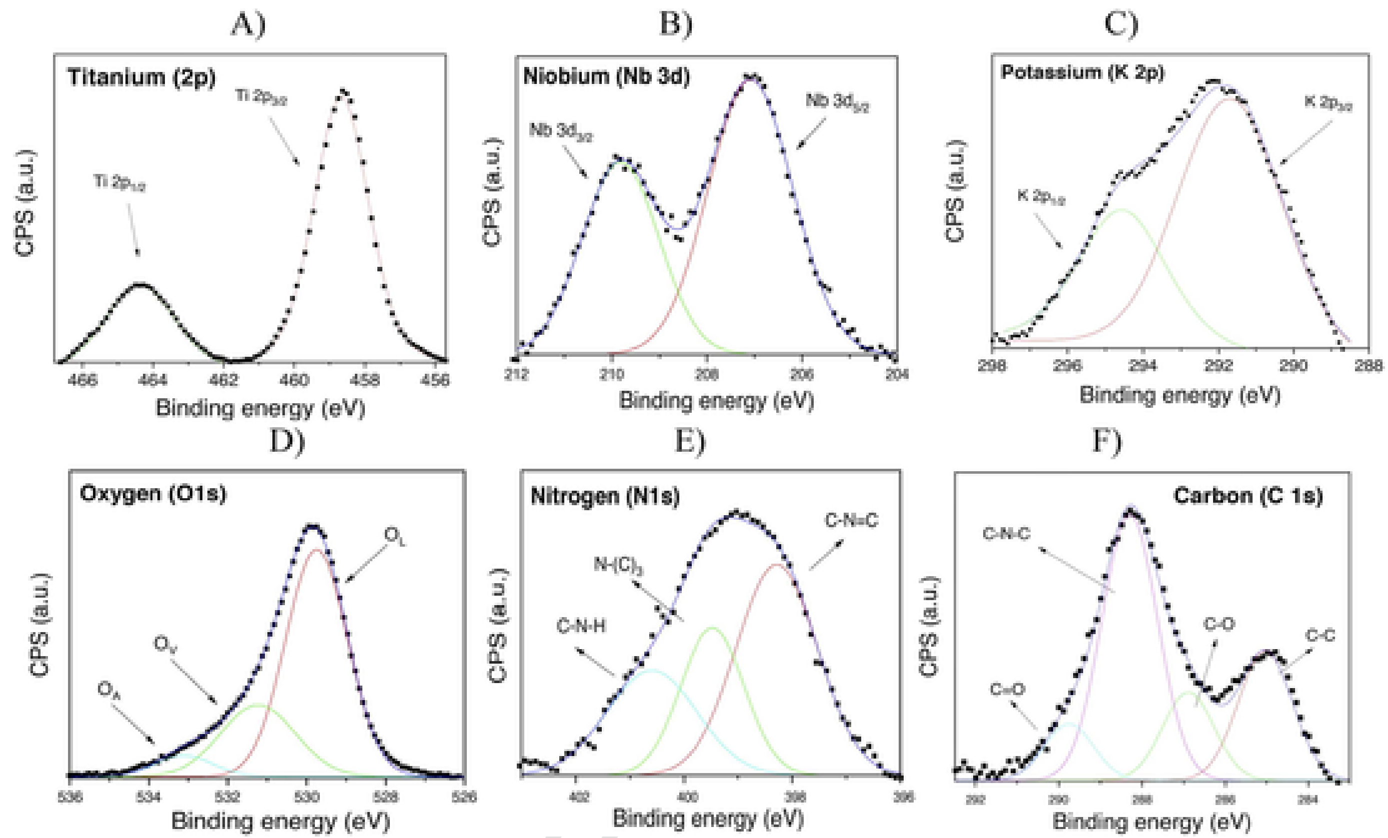

Fig. 2. High-resolution XPS spectra of the TiO_2-5% $KNbO_3$-5% g-C_3N_4 photocatalyst: A) Ti 2p; B) Nb 3d; C) K 2p; D) O 1 s; E) N 1 s; F) C 1 s.

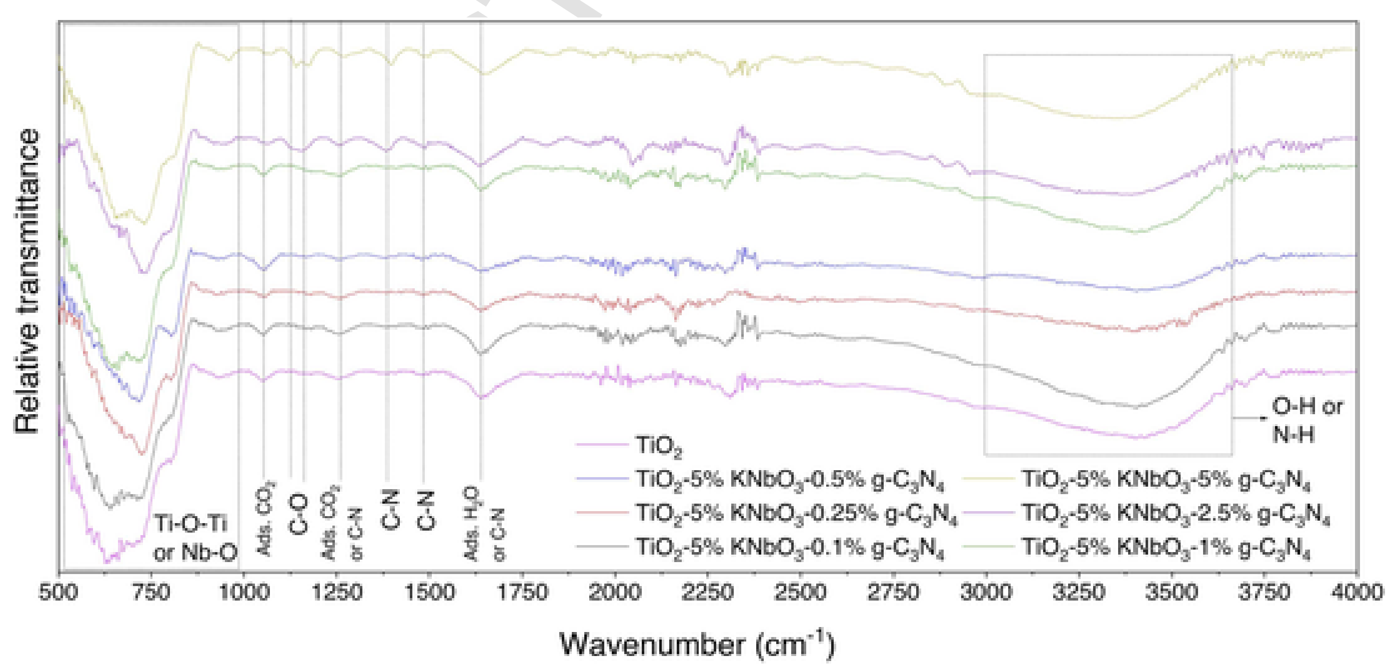

Fig. 3. Infrared spectra of the photocatalysts prepared in this work.

Currently, sunlight-driven heterogeneous photocatalysis has emerged as an innovative and effective technique for the degradation of antibiotics in water treatment processes [8,9]. This process generally utilizes semiconductor materials as photocatalysts to promote chemical reactions under light irradiation [10–12]. When exposed to photons, these catalysts generate electron-hole pairs, initiating a range of redox reactions and producing highly reactive oxygen species, which can rapidly break down antibiotics into non-toxic compounds; this ap-

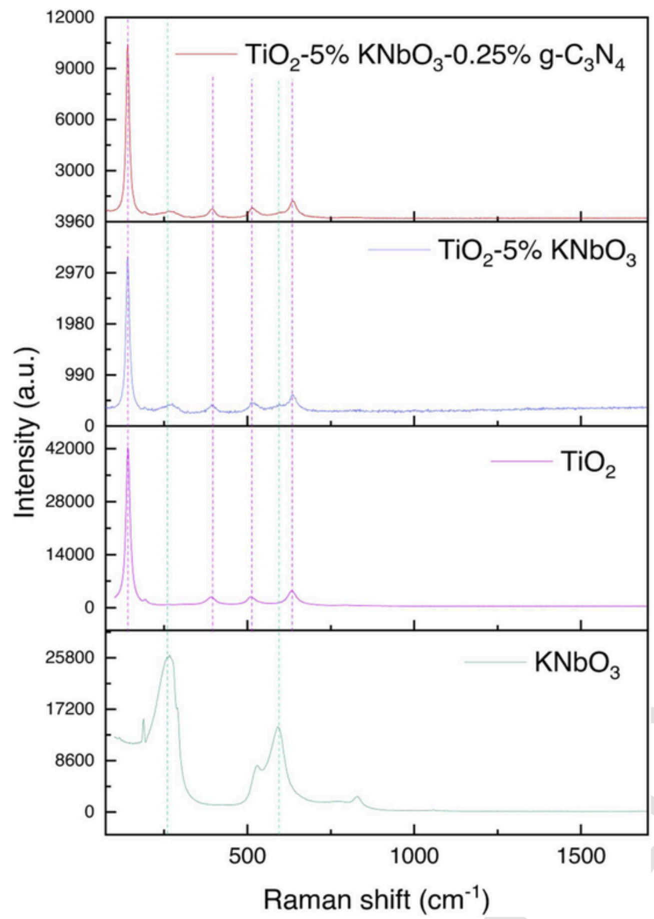

Fig. 4. Raman spectroscopy results for the TiO_2, $KNbO_3$, TiO_2-5% $KNbO_3$, and TiO_2-5% $KNbO_3$-0.25% g-C_3N_4.

proach not only ensures the removal of antibiotic residues but also offers the advantage of minimizing the formation of harmful byproducts [13]. Therefore, heterogeneous photocatalysis offers a sustainable and efficient solution for addressing the detrimental environmental effects of antibiotic contamination in water resources.

In the context of developing highly efficient photodegradation processes, the design of new materials through the creation of heterojunctions between semiconductors has emerged as a primary pathway to boost the overall efficiency of photocatalysts [14,15]. In general, this type of modification promotes a more efficient separation of photogenerated charges during the photoactivation process, diminishing the recombination process and augmenting the photonic efficiency of the developed multi-component photocatalyst [16]. Considering the current state-of-the-art in semiconductor heterojunction design, the Z-scheme heterojunction stands out as a particularly effective strategy [17–19]. This type of heterojunction is based on the creation of an electric field at the semiconductor heterojunction region owing to the formation of electron concentration and depletion regions. This phenomenon directs the recombination between electrons and electron holes formed at the higher potential conduction band and lower potential valence band, respectively. In this way, the electrons and vacancies formed in the outermost conduction and valence bands undergo a separation process and are free to propagate the generation of active radicals [17,18].

Today, titanium dioxide (TiO_2) stands out as the most extensively utilized material in heterogeneous photocatalysis. Therefore, the exploration of new composites involving this semiconductor is of great interest for the development of highly active photocatalytic materials. In this context, the development of Z-scheme heterojunctions with potassium niobate ($KNbO_3$) emerges as a promising alternative for enhancing TiO_2 efficiency during photonic activation. $KNbO_3$ is an n-type semiconductor that exhibits excellent stability, a bandgap energy of approximately 3.2 eV, and a relatively low cost. Additionally, the band structure of potassium niobate is particularly suitable for the formation of Z-scheme heterojunctions with titanium dioxide due to the staggered arrangement of the valence and conduction bands between these materials [20].

However, because of the similarity between the bandgap energies of these semiconductors (≈ 3.2 eV), the response of this binary composite to solar and visible radiation is anticipated to be inadequate. Thus, incorporating a low-bandgap semiconductor into the aforementioned binary material presents a promising solution for enhancing its activity under less energetic light irradiation. In this regard, the semiconductor known as graphitic carbon nitride (g-C_3N_4) is a suitable alternative due to its narrow energy band (2.7 eV), low toxicity, and cost-effective synthesis, commonly achieved through the thermal decomposition of urea [21,22]. The primary drawback of this material is the high recombination rate observed after its photonic excitation; however, the anticipated formation of Z-scheme heterojunctions with both TiO_2 and $KNbO_3$ is expected to effectively mitigate this issue, as the staggered nature of the electronic bands of each of these semiconductors is particularly suitable to promote efficient charge transfer during photonic excitation [23].

In this context, this study focuses on the development of the novel and unreported TiO_2/$KNbO_3$/g-C_3N_4 ternary photocatalyst for application in a sunlight-based photocatalytic process for the degradation of antibiotics, specifically targeting the sulfamerazine compound. To achieve this objective, extensive characterization will be conducted to ascertain the impact of the suggested modifications on the structural, morphological, optical, and photocatalytic attributes of the resulting photocatalysts. Additionally, a thorough analysis of the parameters influencing the degradation efficiency (pH, turbidity, nature of water source) will be performed, along with a comprehensive study of the degradation intermediates obtained and their toxicity. Thus, the information gathered in this paper aims not only to the creation of a new and efficient photocatalyst but also to evaluate the environmental aspects involved in its application, creating a fully contextualized study of photocatalytic processes applied to the degradation of toxic substances.

2. Methodology

2.1. Materials and chemicals

The following materials and chemicals were used in this project: ammonium niobate (V) oxalate hydrate ($C_4H_4NNbO_9 \cdot xH_2O$, 99% w/w, MW = 302.98 g mol^{-1}, CAS Nº 168547–43–1, Companhia Brasileira de Metalurgia e Mineração); potassium hydrogen phthalate ($C_8H_5KO_4$, 99% w/w, MW = 204.22 g mol^{-1}, CAS Nº 877–24–7, Merck); urea (CH_4N_2O, 99% w/w, MW = 60.06 g mol^{-1}, CAS Nº 57–13–6, Neon); hydrofluoric acid (HF, 40% w/w, CAS Nº 7664–39–3, Neon); nitric acid (HNO_3, 65% w/w, CAS Nº 7697–37–2, Synth); ammonium hydroxide solution (1:3 v/v, CAS Nº 1336–21–6, Synth); sodium oxalate (99% w/w, MW = 134 g mol^{-1}, CAS Nº 62–76–0, Neon); potassium chromate (99% w/w, MW = 134 g mol^{-1}, CAS Nº 7789–00–6, Synth); isopropanol (99% w/w, CAS Nº 67–63–0, Synth). Titanium chips were obtained from the machining of titanium-based parts produced in the Department of Materials and Metallurgy of the University of São Paulo.

2.2. Synthesis of the proposed photocatalysts

The potassium niobate used in this study was synthesized based on the methodology proposed by Moraes et al. (2023) [24]. To that intention, 0.056 mol of ammonium niobate (V) oxalate hydrate and 0.056 mol of potassium hydrogen phthalate were solubilized in 5 mL of

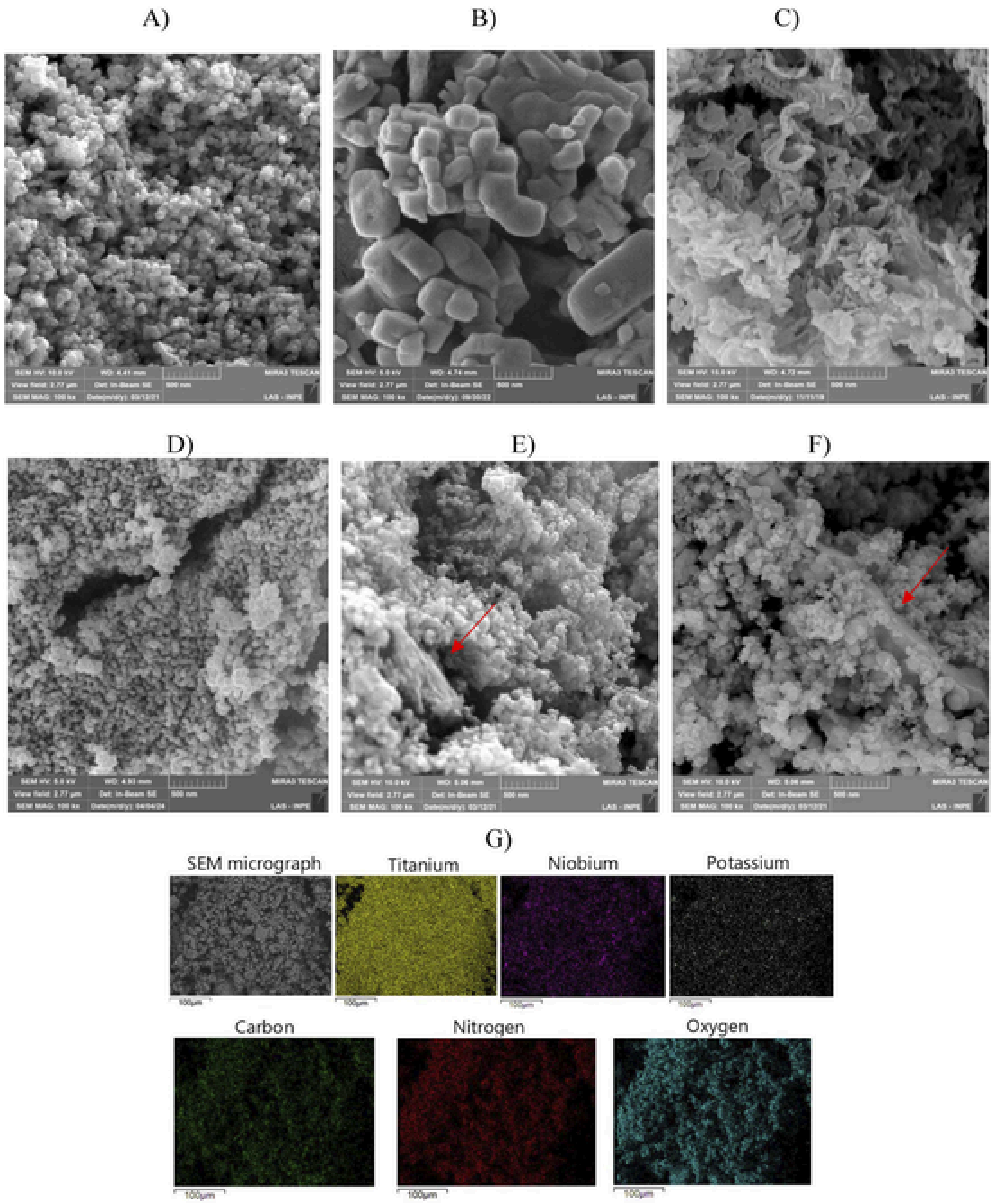

Fig. 5. Scanning electron micrographs for: A) TiO_2; B) $KNbO_3$; C) g-C_3N_4; D) TiO_2-5% $KNbO_3$; E) TiO_2-0.25% g-C_3N_4; F) TiO_2-5% $KNbO_3$-0.25% g-C_3N_4; G) Elemental mapping for the TiO_2-5% $KNbO_3$-0.25% g-C_3N_4 ternary composite.

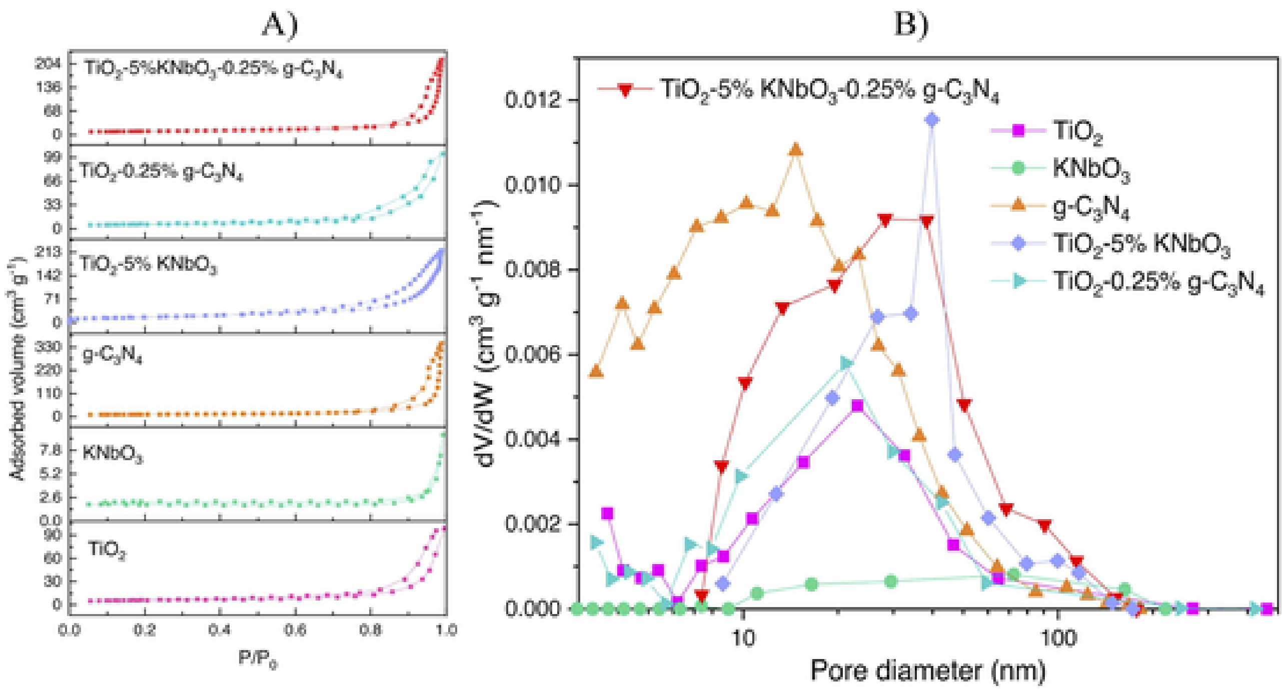

Fig. 6. A) Nitrogen adsorption-desorption isotherms obtained for the TiO_2, $KNbO_3$, g-C_3N_4, TiO_2-5% $KNbO_3$, and TiO_2-5% $KNbO_3$-0.25% g-C_3N_4; B) Pore size distribution for the TiO_2, $KNbO_3$, g-C_3N_4, TiO_2-5% $KNbO_3$, and TiO_2-5% $KNbO_3$-0.25% g-C_3N_4.

Table 2 -
Specific surface area (SSA) and pore volume (PV) calculated for the TiO_2, $KNbO_3$, g-C_3N_4, TiO_2-5% $KNbO_3$, TiO_2-0.25% g-C_3N_4 and TiO_2-5% $KNbO_3$-0.25% g-C_3N_4.

Material	SSA (m^2 g^{-1})	Micropore SSA (m^2 g^{-1})	PV (cm^3 g^{-1})	Micropore PV (cm^3 g^{-1})
TiO_2	19.40	10.30	0.15	0.0048
$KNbO_3$	6.00	-	0.014	-
g-C_3N_4	60.03	2.11	0.34	0.0009
TiO_2-5%$KNbO_3$	35.25	8.74	0.33	0.0041
TiO_2-0.25% g-C_3N_4	21.50	11.40	0.17	0.0051
TiO_2-5% $KNbO_3$-0.25% g-C_3N_4	35.45	11.42	0.54	0.0053

deionized water inside a porcelain crucible. The crucible containing the solution was then placed into a muffle furnace and calcined at 600 ºC for 2 h. The graphitic carbon nitride (g-C_3N_4) was synthesized based on the methodology proposed by Sousa et al. (2020), through the thermal treatment of 10 g of urea within a lidded crucible [25]. The process was executed in a muffle furnace, maintained at a temperature of 550 ºC for 2 hours, with a heating rate of 10 ºC min^{-1}.

The ternary photocatalyst was synthesized as follows: first, 1.5 g of titanium chips and 10 mL of deionized water were added to a polypropylene beaker. Subsequently, 4 mL of 40% w/w hydrofluoric acid was added to the system, followed by the dropwise addition of 1.5 mL of 65% w/w nitric acid [26]. After the complete dissolution of the titanium, the volume of the resulting solution was adjusted to 100 mL. The pH of the titanium solution was adjusted to 4 using an ammonium hydroxide solution (1:3 v/v). Then, pre-defined amounts of $KNbO_3$ and g-C_3N_4 were added to the titanium solution, which was kept under magnetic stirring. To promote the precipitation of the composites, 45 mL of ammonium hydroxide solution (1:3 v/v) was added to the system. The resulting precipitates were then separated by filtration and washed with deionized water until pH = 7. After drying for 24 h in an oven (100 ºC), the materials were sifted using a 325-mesh analytical sieve. Finally, the materials were added to lidded crucibles and calcined in a muffle furnace at 500 ºC for 1 h (heating rate of 10 ºC min^{-1}) under a nitrogen atmosphere (0.5 L min^{-1}). The materials produced were named TiO_2-w% $KNbO_3$-y% g-C_3N_4, where w% and y% represent the theoretical mass fractions of $KNbO_3$ and g-C_3N_4, respectively, in the composites. The inventory of reactants and the respective amounts employed in the production of each photocatalyst are listed in Table S1.

2.3. Characterization and photocatalytic tests

Detailed information about the characterization methods and the equipment used can be found in the supplementary material. The photocatalytic experiments were conducted using a jacketed reactor with dimensions of 10 cm in height and 10 cm in internal diameter. In this reactor, 0.5 L of sulfamerazine solution (C_0 = 10 mg L^{-1}) was introduced along with 0.05 g of photocatalyst, which was evenly dispersed via magnetic stirring. To maintain the process at a constant temperature of 25 ºC, a thermostatic bath was used to pump cooling water through the reactor's jacket. The concentration of sulfamerazine was determined by a straightforward spectrophotometric technique using a Shimadzu UV-2600 spectrophotometer. This measurement utilized a wavelength of 262 nm for SFMZ detection, as determined from the absorption spectrum of SFMZ and relevant literature [27–29]. To validate this approach, the concentration of sulfamerazine was also assessed through high-performance liquid chromatography (HPLC). For this purpose, a Shimadzu HPLC model LC-20 AT was employed, equipped with a Phenomenex Luna C-18 column and a mobile phase consisting of 30% water and 70% acetonitrile. A flow rate of 1 mL min^{-1} was maintained, with an injection volume of 20 μL and a retention time of 10 min. The measurements were conducted using a UV detector set to a wavelength of 270 nm [30,31]. Total organic carbon (TOC) was measured using Shimadzu VCSN TOC equipment. Before commencing the photocatalytic experiments, the reactor was maintained in the dark until adsorption-desorption equilibrium was established. Subsequently, the samples were exposed to artificial radiation sources, either solar or visible. An Osram Ultra Vitalux 300 W lamp was utilized to mimic sunlight, while

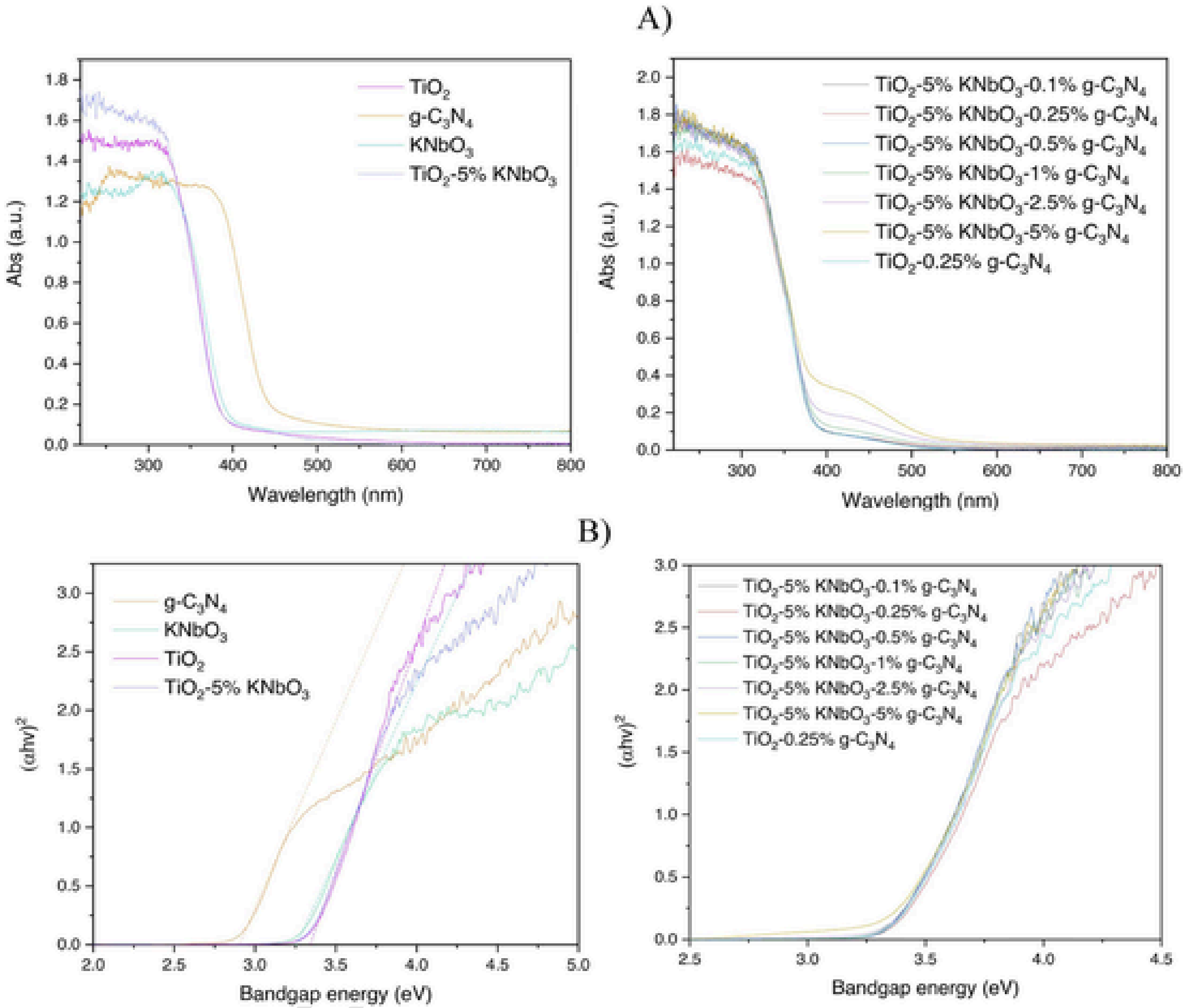

Fig. 7. – A) Diffuse reflectance spectra of the photocatalysts; B) Kubelka-Munk plots.

an OSRAM Powerstar 400 W lamp equipped with a UV filter served as the visible light source. To evaluate the photocatalytic mechanism of active radical generation, scavenging tests were conducted in the presence of various substances: isopropanol (5% v/v, scavenger for hydroxyl radicals), nitrogen (inhibitor of superoxide radicals, 0.3 L min^{-1}), sodium oxalate (scavenger for electron holes, 0.5 mol L^{-1}), and potassium chromate (scavenger for e^-, 0.025 mol L^{-1}) [32]. Turbidity tests were performed by the addition of montmorillonite clay, whereas the variation of pH was obtained using 0.1 M solutions of HCl and NaOH.

The degradation products were identified by liquid chromatography-electrospray triple quadrupole spectrometry (LC-ESI-MS/MS 8030, Shimadzu). A Shim-pack GIST C18 reverse phase column (Shimadzu) was employed. Acetonitrile (A) and water (B), both acidified with 0.1% formic acid, were used as the mobile phase at a flow rate of 0.6 mL min^{-1}. The elution mode was linear gradient (0–5 min: 10–37%; 5–8 min: 37–100%; after 8–10 min of post-run time, the composition of the mobile phase was returned to the initial condition). Positive electrospray ionization mode (ESI +) was used for the analysis. The spray voltage (+) was 3.5 kV, and the capillary and source block temperatures were 250 ˚C and 400 ˚C, respectively. Nitrogen was applied as a nebulizer and desolvation gas at flow rates of 3 L min^{-1} and 15 L min^{-1}, respectively.

3. Results and discussions

3.1. Characterization

Fig. 1 shows the results of the X-ray diffractometry (XRD) of the materials synthesized, whereas Table 1 lists the parameters obtained from the Rietveld refinement of XRD data.

Firstly, by analyzing Fig. 1 A, it is possible to observe that all of the pure semiconductors proposed were successfully synthesized. Considering that, the TiO_2 prepared is composed solely of the anatase tetragonal crystalline structure (JCPDS Card no. 21–1272), whereas the $KNbO_3$ prepared presents the peaks related to the orthorhombic crystalline structure (JCPDS Card no. 32–0822). The g-C_3N_4 displayed one major peak in the 2θ region evaluated, centered at approximately 27.6º, which is related to the (002) plane (*d*-spacing of 0.326 nm) linked to the distance between layers of the graphitic carbon nitride [33,34]. Additionally, a smaller peak located at approximately 13 º can be observed, related to the layered structure of stacked triazine units [35].

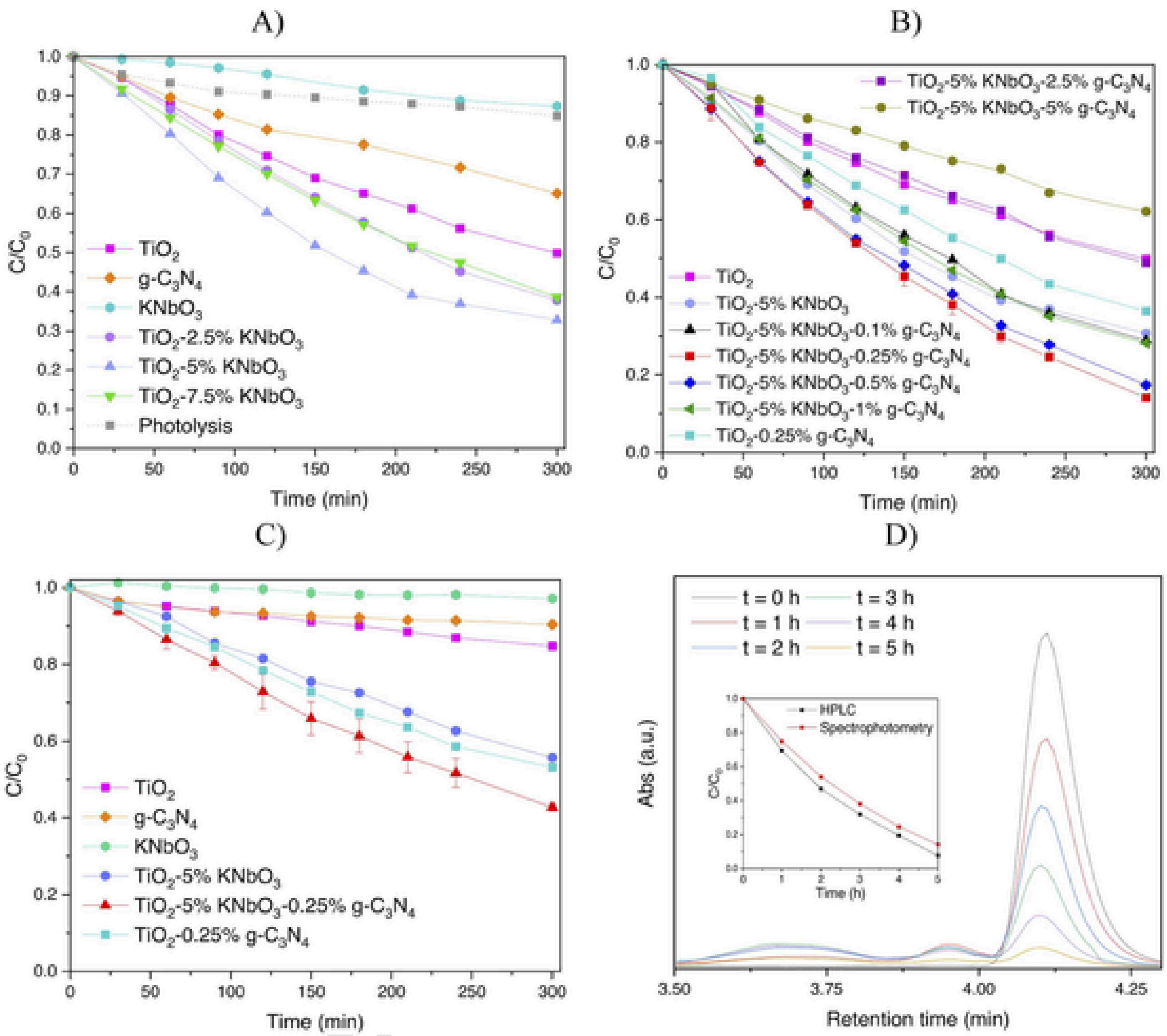

Fig. 8. – A) SFMZ photodegradation using TiO_2, g-C_3N_4, $KNbO_3$ and TiO_2-w% $KNbO_3$ (artificial sunlight); B) SFMZ photodegradation using TiO_2-w% $KNbO_3$-y% g-C_3N_4 composites (artificial sunlight); C) Efficiency of the optimized photocatalysts under visible light; D) HPLC results for the SFMZ photodegradation using the TiO_2-5% $KNbO_3$-0.25% g-C_3N_4 (artificial sunlight).

Table 3 –
Kinetic data obtained through the pseudo-first-order kinetic model.

Photocatalyst	Simulated sunlight		Visible light	
	k_{app} (min $^{-1}$)	R^2	k_{app} (min $^{-1}$)	R^2
TiO_2	0.0024	0.998	0.0005	0.986
$KNbO_3$	0.0005	0.981	0.0001	0.965
g-C_3N_4	0.0014	0.988	0.0003	0.962
TiO_2-2.5% $KNbO_3$	0.0034	0.995	-	-
TiO_2-5% $KNbO_3$	0.0040	0.987	0.0020	0.996
TiO_2-7.5% $KNbO_3$	0.0032	0.994	-	-
TiO_2-0.25% g-C_3N_4	0.0031	0.991	0.0023	0.995
TiO_2-5% $KNbO_3$-0.1% g-C_3N_4	0.0043	0.995	-	-
TiO_2-5% $KNbO_3$-0.25% g-C_3N_4	0.0065	0.987	0.0029	0.998
TiO_2-5% $KNbO_3$-0.5% g-C_3N_4	0.0057	0.991	-	-
TiO_2-5% $KNbO_3$-1% g-C_3N_4	0.0044	0.997	-	-
TiO_2-5% $KNbO_3$-2.5% g-C_3N_4	0.0024	0.997	-	-
TiO_2-5% $KNbO_3$-5% g-C_3N_4	0.0016	0.995	-	-

As for the binary TiO_2-w% $KNbO_3$ photocatalysts (Fig. 1B), both tetragonal TiO_2 and orthorhombic $KNbO_3$ structures were present in the diffractograms collected, as expected. Furthermore, the Rietveld refinement of the samples shows that a higher theoretical $KNbO_3$ mass fraction is linked to an increase in the experimental $KNbO_3$ mass fraction. The difference between the theoretical and experimental mass fractions can be explained by the fact that Rietveld refinement is a semi-quantitative technique, and deviations are expected due to the different X-ray absorption coefficients presented by each atom in the structure of the developed materials [36].

Finally, the X-ray diffractograms of the ternary TiO_2-5% $KNbO_3$-y% g-C_3N_4 and binary TiO_2-0.25% g-C_3N_4 showed only the tetragonal TiO_2 and orthorhombic $KNbO_3$ structures observed previously, with no defined peak related to the graphitic carbon nitride. As shown in Fig. 1 A, the intensity of the diffractogram obtained for the g-C_3N_4 is much lower than the ones observed for the TiO_2 and $KNbO_3$ and, therefore, it is probable that the mass fractions of g-C_3N_4 chosen for the ternary photocatalysts (0.1–5%) were not sufficient to render an observable signal for this component [37]. However, it is noticeable that higher fractions of

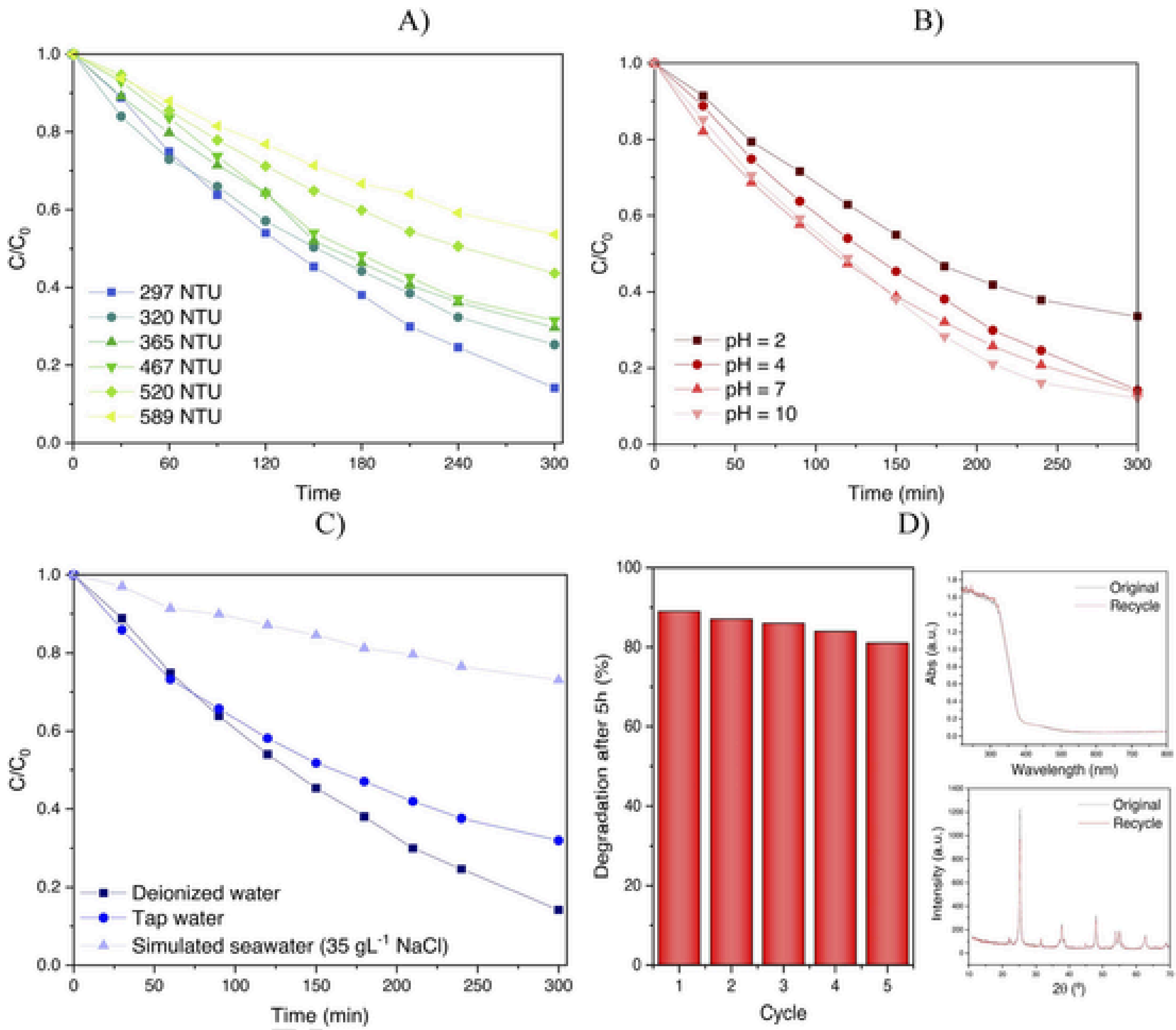

Fig. 9. – A) Influence of turbidity on the SFMZ degradation; B) Influence of pH on the SFMZ degradation; C) Influence of the nature of the aqueous medium on the SFMZ degradation; D) Recycle results for the TiO_2-5% $KNbO_3$-0.25% g-C_3N_4.

g-C_3N_4 can be directly related to a reduction in the apparent crystallite size (L_c) of the TiO_2 structure, as shown in Table 1. Thus, it is clear that higher amounts of the g-C_3N_4 influenced significantly the crystallization process of the TiO_2, which is probably linked to the fact that the g-C_3N_4 particles present during the synthesis pathway may function as nucleating sites for the TiO_2 particles, resulting in smaller crystallite sizes [38].

Fig. 2 shows the high-resolution X-ray photoelectron spectroscopy (XPS) spectra obtained for the TiO_2-5% $KNbO_3$-5% g-C_3N_4, aiming to better understand the resulting structure of the developed ternary photocatalysts.

As expected, six main elements (Ti, Nb, K, O, N, and C) were identified by the XPS analysis of the TiO_2-5% $KNbO_3$-5% g-C_3N_4 photocatalyst. Observing Fig. 2 A, the occurrence of Ti $2p_{1/2}$ and Ti $2p_{3/2}$ modes at 458.6 and 464.4 eV, respectively, aligns with the expected signature of the Ti^{4+} atoms in the TiO_2 tetragonal structure. [39]. The Nb 3d spectrum (Fig. 2B) exhibits a pair of peaks at 207 eV and 210 eV, which correspond to the binding energies of the Nb $3d_{5/2}$ and Nb $3d_{3/2}$ modes, respectively. This finding can be attributed to the presence of Nb^{5+} in the orthorhombic structure of the $KNbO_3$ phase [24]. For the potassium spectrum (Fig. 2 C), the resulting data could be deconvoluted into two bands, which are reportedly linked to the $2p_{1/2}$ and $2p_{3/2}$ modes of the K^+ atom of the orthorhombic $KNbO_3$ phase [40].

Considering the O 1 s spectrum (Fig. 2D), three main peaks could be deconvoluted: the first and more intense peak (O_L, ≈ 529.7 eV) can be associated with the surface lattice oxygen atoms of both the TiO_2 and $KNbO_3$ structures, whereas the second (O_V, ≈ 531.2 eV) and third peaks (O_A, ≈ 533.1 eV) are likely resultant from the presence of oxygen vacancies and hydroxyl (O-H) groups, respectively [41,42]. The nitrogen spectrum (Fig. 2E) was also deconvoluted into three peaks, which can be attributed to triazine rings (298.3 eV), tertiary nitrogen (399.5 eV), and amino groups (400.6 eV) derived from the carbon nitride structure [37,43]. Lastly, the C1s spectrum (Fig. 2 F) was deconvoluted into four

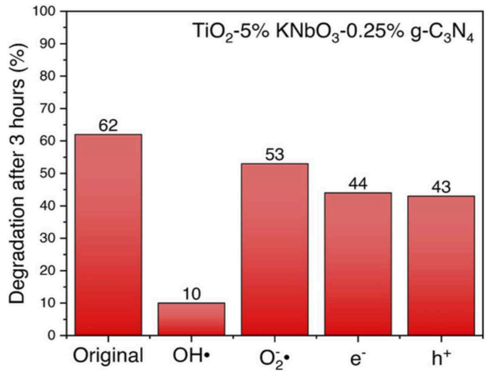

Fig. 10. – Scavenger tests for the TiO_2-5% $KNbO_3$-0.25% g-C_3N_4 (under artificial sunlight).

Table 4 –
Conduction and valence band levels found for the semiconductors.

Semiconductor	E_{CB} (eV)	Ev_B (eV)
TiO_2	-0.35	2.98
g-C_3N_4	-1.22	1.68
$KNbO_3$	-0.85	2.40

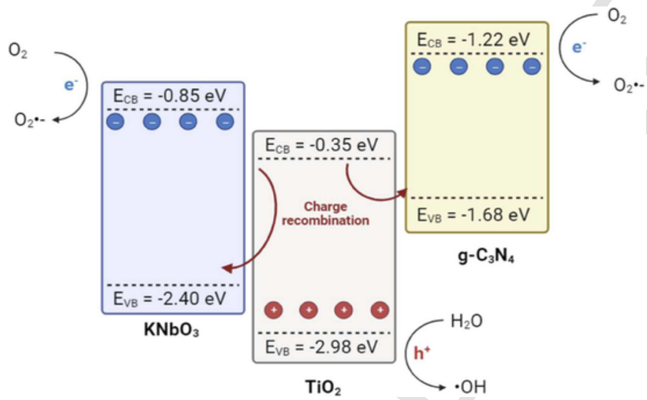

Fig. 11. - Global mechanism of charge transfer for the photocatalytic process.

peaks. The most intense peak, located at approximately 288.2 eV, is related to the sp ^{2}-bonded N═C–N linkage found in the g-C_3N_4 structure, whereas the peaks at 286.7 and 289.7 eV suggest the presence of oxygenated C-O and C═O species on the surface of the carbon nitride, respectively. The peak located at 284.7 eV can be assigned to C–C bonds derived from adventitious carbon present during the analysis [43].

Fig. 3 shows the infrared spectra (IR) obtained for the photocatalysts prepared aiming to further evaluate the chemical structure of the samples.

Considering the nature of the synthesized photocatalysts, the following information can be extracted from the infrared spectra collected. First, the bands located in the region between 500 and 900 cm^{-1} can be related to the Ti-O-Ti lattice vibrations derived from the titanium dioxide in the samples or the Nb-O octahedra from the $KNbO_3$ [44,45]. Furthermore, bands with low intensity were observed for all samples at approximately 1064 and 1250 cm^{-1}, which can be related to the surface carbonate species formed by the adsorption of atmospheric CO_2 [44]. Regarding the presence of nitrogen-containing groups, the bands located at approximately 1380 and 1480 cm^{-1} can be related solely to the presence of C-N groups on the surface of the materials and, as expected, these bands can be observed with more intensity in the photocatalysts with a higher carbon nitride mass fraction [46]. Additionally, a higher g-C_3N_4 content leads to the appearance of C-O bands at 1140 and 1170 cm^{-1}, corroborating the presence of oxygenated groups on the surface of the g-C_3N_4 as observed by XPS analysis [47]. Finally, the band located at 1620 cm^{-1} can be related to both adsorbed water molecules and C═N bonds, whereas the large band centered at approximately 3350 cm^{-1} can be linked to the presence of O-H and/or N-H groups [46,48].

Fig. 4 shows the Raman spectroscopy results for the TiO_2, $KNbO_3$, TiO_2-5% $KNbO_3$, and TiO_2-5% $KNbO_3$-0.25% g-C_3N_4.

As shown in Fig. 4, the Raman spectrum of the synthesized potassium niobate is characteristic of its orthorhombic structure, as the following modes can be distinctly observed: $B_1(TO_2)$ (190 cm^{-1}), $B_1(TO_1)$ (245.3 cm^{-1}), $B_1(TO_3)$ (531 cm^{-1}), $A_1(TO_3)$ (598 cm^{-1}), and $A_1(LO_3)$ (832 cm^{-1}) [49]. The pure TiO_2 spectrum also agrees with the information obtained by X-ray diffractometry, as the modes characteristic of its tetragonal structure can be observed at 141 cm^{-1} ($E_{g(1)}$), 369 cm^{-1} ($B_{1\ g(1)}$), 510 cm^{-1} ($A_{1\ g}$ + $B_{1\ g(2)}$), and 635 cm^{-1} ($E_{g(2)}$) [50]. Both the TiO_2-5% $KNbO_3$ and TiO_2-5% $KNbO_3$.0.25% g-C_3N_4 display a mixture of the modes observed for the pure TiO_2 and $KNbO_3$, in a similar manner to the X-ray diffractograms, confirming the presence of these structures on the developed composites. However, no characteristic peaks of g-C_3N_4 could be observed for the ternary material, probably due to the low mass fraction of this compound in the analyzed sample.

Fig. 5 shows the scanning electron micrographs for TiO_2, $KNbO_3$, g-C_3N_4, TiO_2-5% $KNbO_3$, and TiO_2-5% $KNbO_3$-0.25% g-C_3N_4 and the elemental mapping obtained for TiO_2-5% $KNbO_3$-0.25% g-C_3N_4.

The micrograph of pure TiO_2 (Fig. 5 A) shows that it is morphologically composed of small nodular particles, which are distributed in the form of particle agglomerates. The $KNbO_3$, on the other hand, is composed of cuboid-like particles with larger sizes (Fig. 5B), especially when compared to the pure TiO_2 particles. As reported in previous literature, this behavior is characteristic of $KNbO_3$ perovskites synthesized through a wide range of different methodologies, including hydrothermal, solid-state, and Pechini pathways [51–55]. Fig. 5 C shows that g-C_3N_4 consists of non-uniform flake-like particles, which is also a characteristic morphology commonly observed for this particular material [56]. The binary and ternary composites maintained the morphology displayed by the pure TiO_2; however, it can be observed in the highlighted regions that the nodular particles are likely deposited on the surface of larger particles, indicating that the TiO_2 is covering the $KNbO_3$ and g-C_3N_4 particles. Considering the proposed synthesis pathway, this conclusion is quite straightforward, as the TiO_2 component is precipitated on top of the $KNbO_3$ and g-C_3N_4 particles dispersed in the aqueous reaction medium.

The elemental mapping obtained for the TiO_2-5% $KNbO_3$-0.25% g-C_3N_4 (Fig. 5 F) shows that, overall, the composing elements of the individual semiconductors forming the ternary composite are well distributed throughout its surface. This feature is well suited for enhancing the charge transfer efficiency within the heterojunctions formed among the chosen semiconductors, leading to a reduction in the recombination of photogenerated charges and consequently boosting the photocatalytic activity of the composite [57].

Fig. 6 shows the nitrogen adsorption-desorption isotherms and pore-size distribution obtained for the materials, whereas Table 2 lists the morphological parameters obtained using the methodologies described in Section 2.2.

Fig. 6A shows that all the nitrogen adsorption-desorption isotherms present the same behavior, which, according to IUPAC classification, is characteristic of type IV isotherms with an H3 hysteresis loop [58]. Type IV isotherms are observed in the case of mesoporous materials (where the pore size falls within the range of 2 nm to 50 nm), whereas the presence of a H3 hysteresis loop is connected to

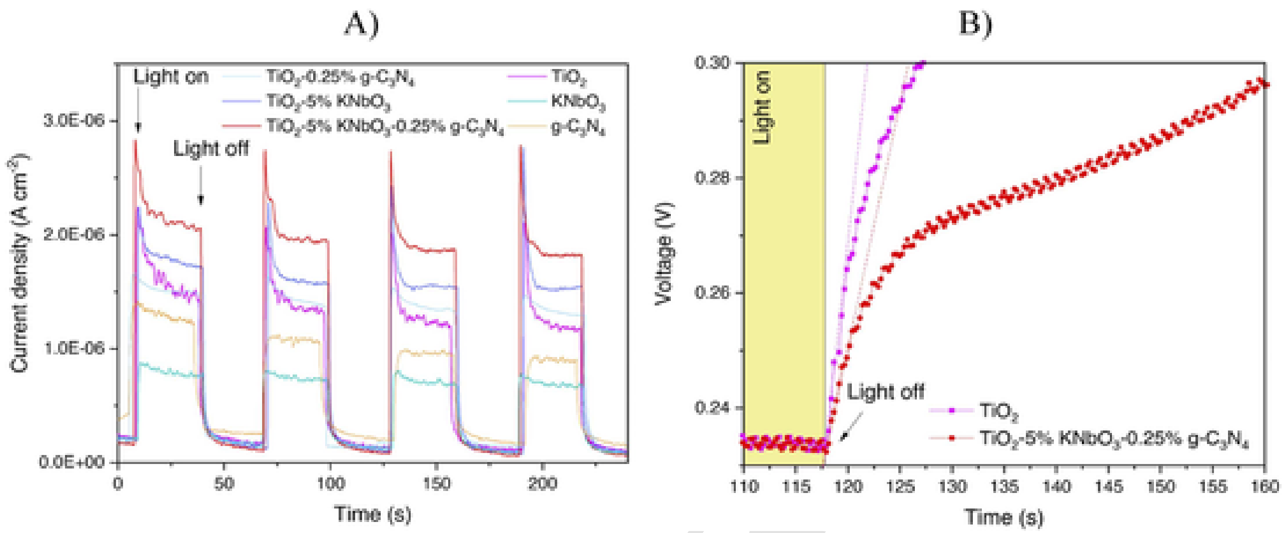

Fig. 12. - A) Chronoamperometry tests for the photocatalysts (under simulated sunlight); B) OCP tests for the TiO_2 and TiO_2-5% $KNbO_3$-0.25% g-C_3N_4 (under simulated sunlight).

Table 5 -
Products generated during sulfamerazine degradation using the TiO_2-5% $KNbO_3$-0.25% g-C_3N_4 (under simulated sunlight).

Degradation product	Formula	RT (min)	Molecular Ion $[M+H]^+$	Fragment Ions *(m/z)*
1	$C_4H_{10}N_2O_4S$	0.11	183	130, 110, 102
2	$C_{10}H_{14}N_4$	0,59	191	167, 122, 102
3	$C_{10}H_{13}N_3O_2$	0.64	208	167, 123, 102
4	$C_4H_6O_6$	1.50	151	100, 83
5	$C_{10}H_{14}N_4O_4S$	3.38	287	265, 100
6	$C_5H_7N_3O_2$	5.58	142	100, 83
7	$C_{10}H_{15}N_3O_4S$	6.63	274	100, 83
8	$C_{11}H_{10}N_4O_3S$	7.39	279	100, 83

the phenomenon of capillary condensation on solids with a very wide pore size distribution [59].

Considering the pure TiO_2, Table 2 shows that the inclusion of the $KNbO_3$ (TiO_2-5% $KNbO_3$) led to a significant increase in both the specific surface area and pore volume of the binary composite, which is a favorable modification due to the increased interface available for the propagation of superficial phenomena, such as the photocatalytic activation and adsorption process [60]. This increase can be related to the formation of a more developed mesopore structure, especially in the region between 20 nm and 100 nm (Fig. 6B). The further inclusion of the g-C_3N_4, in the form of the TiO_2-5% $KNbO_3$-0.25% g-C_3N_4 composite, resulted in no major effect on the specific surface area of the photocatalyst, even though a greater pore volume was achieved. Regarding the pore distribution of the ternary composite, the addition of both the $KNbO_3$ and g-C_3N_4 led to the enhanced formation of pores ranging from 5 nm to 100 nm. The increase in pores ranging from 5 to 20 nm could be ascribed to the presence of the g-C_3N_4, as the pore distribution of the pure carbon nitride is concentrated in this region.

Fig. 7 shows the diffuse reflectance spectra (DR) and Kubelka-Munk plots obtained for the determination of the bandgap energy (E_{gap}) of photocatalysts developed, using the Kubelka-Munk function and Tauc plots [61].

Firstly, it is possible to observe from the results displayed in Fig. 7B that the calculated bandgap energies for the pure semiconductors (E_{gap} (TiO_2) = 3.33 eV, E_{gap} ($KNbO_3$) = 3.25 eV and E_{gap} (g-C_3N_4) = 2.9 eV) are within the expected values, as reported by related literature [25,26, 62]. Furthermore, the addition of both the $KNbO_3$ and g-C_3N_4 did not lead to any major modification to the bandgap of the binary and ternary photocatalysts, as all these materials presented bandgap energies of approximately 3.3 eV. However, it can be observed for the TiO_2-5% $KNbO_3$-y% g-C_3N_4 that a new absorption band emerges between 400 nm and 500 nm for the materials with higher g-C_3N_4 mass fractions, further confirming the presence of this component in the ternary photocatalysts.

3.2. *Photocatalytic evaluation*

Fig. 8 shows the evaluation of the photocatalytic performance of the materials synthesized for sulfamerazine degradation under simulated sunlight and visible light.

First, it is necessary to point out that all of the catalysts evaluated in this work displayed a negligible adsorption capacity for the sulfamerazine molecule. Fig. 8A shows that the incorporation of the potassium niobate into the titanium dioxide was favorable for enhancing the photocatalytic activity of the binary composite material. This result is derived from the heterojunctions formed between the two semiconductors, which can facilitate charge transfer during photonic activation and hinder the charge recombination process. Additionally, the increase in the specific surface area observed for the TiO_2-5% $KNbO_3$ is also favorable in the context of its photocatalytic efficiency, as a larger interface will be available to propagate the reaction steps involved in the photocatalytic degradation process. Furthermore, it is worth pointing out that both $KNbO_3$ and g-C_3N_4 displayed inferior photocatalytic activity compared to the TiO_2, which may be related to the low specific area found for the $KNbO_3$ and the high recombination rates of g-C_3N_4 during photonic activation, as previously reported by related literature [25]. The best photocatalytic activity was found for the TiO_2-5% $KNbO_3$; thus, this composition was employed to produce the ternary composite.

Fig. 8B exhibits that the inclusion of the graphitic carbon nitride to both the TiO_2 and the TiO_2-5% $KNbO_3$ led to a further enhancement of the photocatalytic efficiency of sulfamerazine degradation, especially for the TiO_2-5% $KNbO_3$-0.25% g-C_3N_4 ternary composite, which obtained 86.5% removal and 55% TOC removal after 5 h. This could be explained by both the formation of double heterojunctions with TiO_2 and the visible-light activity of g-C_3N_4, which has a low bandgap energy. Note that the optimal composition of the g-C_3N_4 was considerably lower than that of the $KNbO_3$, which can be explained by the very low density and high surface area of the g-C_3N_4, creating a functional heterojunction interface region even with low amounts

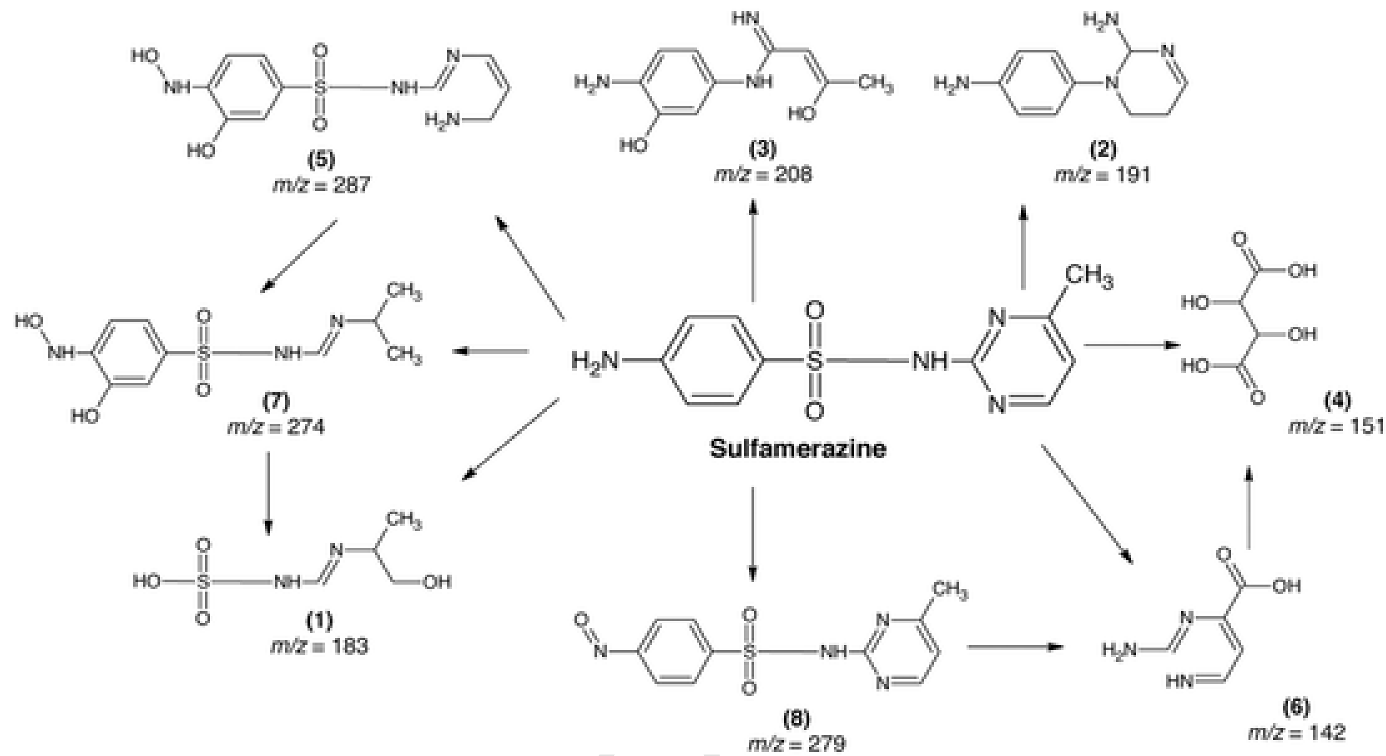

Fig. 13. - Proposed degradation pathway and structure of identified products formed during the photocatalytic degradation of the sulfamerazine molecule.

of the semiconductor. A similar result was reported by Sousa et al. (2020), where the optimal carbon nitride composition for the ZnO/g-C_3N_4/carbon xerogel composite was also 0.25% w/w [25]. As for the visible-light tests, Fig. 8C shows that the inclusion of both $KNbO_3$ and g-C_3N_4 was favorable to the photocatalytic activity of the TiO_2 under visible light irradiation, considering that the pure TiO_2 has very low activity when irradiated with such wavelengths, as expected. This is once again probably derived from the facilitated charge transfer between the semiconductors and the low bandgap of the g-C_3N_4. Finally, the HPLC results displayed in Fig. 8D show a similar degradation profile as the one obtained through simple spectrophotometry measurements, indicating that the formation of byproducts during the process did not cause a significant deviation in the proposed measurements.

The data collected from the photocatalytic tests were fitted using a pseudo-first-order kinetic model, which is described by Eq. 1 and is based on the Langmuir-Hinshelwood equation [63]:

$$\ln\left(\frac{C_0}{C}\right) = k_{app}t \quad (1)$$

where C_0 is the concentration at the adsorption equilibrium and k_{app} is the apparent rate constant, which can be defined as the slope of the ln (C_0/C) versus t plot.

The kinetic data pertaining to the suggested model are showcased in Table 3.

The kinetic parameters derived from the photocatalytic reactions indicate the appropriateness of the proposed kinetic model for describing the evaluated photocatalytic process, which is supported by the fact that all the R^2 values were close to 1. Specifically, the TiO_2-5% $KNbO_3$-0.25% g-C_3N_4 sample demonstrated the highest k_{app} values in both solar and visible-light photocatalytic tests, reaffirming its status as the most effective photocatalyst among the materials examined in this study.

Fig. 9 aims to evaluate the influence of multiple operational parameters on the overall degradation of the sulfamerazine molecule by the TiO_2-5% $KNbO_3$-0.25% g-C_3N_4, such as pH, turbidity, the nature of the aqueous medium and recycling tests. All tests were conducted using the same methodology proposed in Section 2.3, under simulated sunlight.

Fig. 9A illustrates that a higher turbidity in the system correlates with a lower degradation rate of SFMZ. As expected, this relationship occurs due to the presence of the montmorillonite during the photocatalytic tests, which hampers light penetration [64]. Observing the results, it is noticeable that a major efficiency drop only occurred after the turbidity of the system reached 520 NTU, indicating that the process can be carried out with reasonable efficiency in aqueous effluents with turbidity in the range between 297 and 467 NTU.

Regarding the pH of the system, Fig. 9B indicates that higher pH values result in improved removal efficiency for the SFMZ. This result can be elucidated by the increased presence of hydroxyl anions in the solution, which would likely promote an increased generation of active hydroxyl radicals during the photocatalytic process [65]. It can also be noted that the nature of the aqueous medium had a significant influence on the degradation of the SFMZ. Fig. 9C demonstrates that using unpurified water led to a reduced efficiency in the degradation process, particularly noticeable when simulated seawater was used. This outcome could be attributed to the hydroxyl scavenger effect promoted by cations and anions present in unpurified water matrices, such as those derived from sodium chloride. This scavenger effect is known to hinder the efficiency of advanced oxidation processes (AOPs) based on the generation of hydroxyl radicals [66,67]. Finally, Fig. 9D shows that the TiO_2-5% $KNbO_3$-0.25% g-C_3N_4 has good recycling properties, losing approximately 2% of efficiency between cycles; furthermore, the XRD and DR analyses after recycling show that no major structural and optical modifications were observed.

In order to evaluate the mechanism of active radical generation and charge transfer in the developed TiO_2-5% $KNbO_3$-0.25% g-C_3N_4 ternary material, scavenger tests were conducted. The results are shown in Fig. 10.

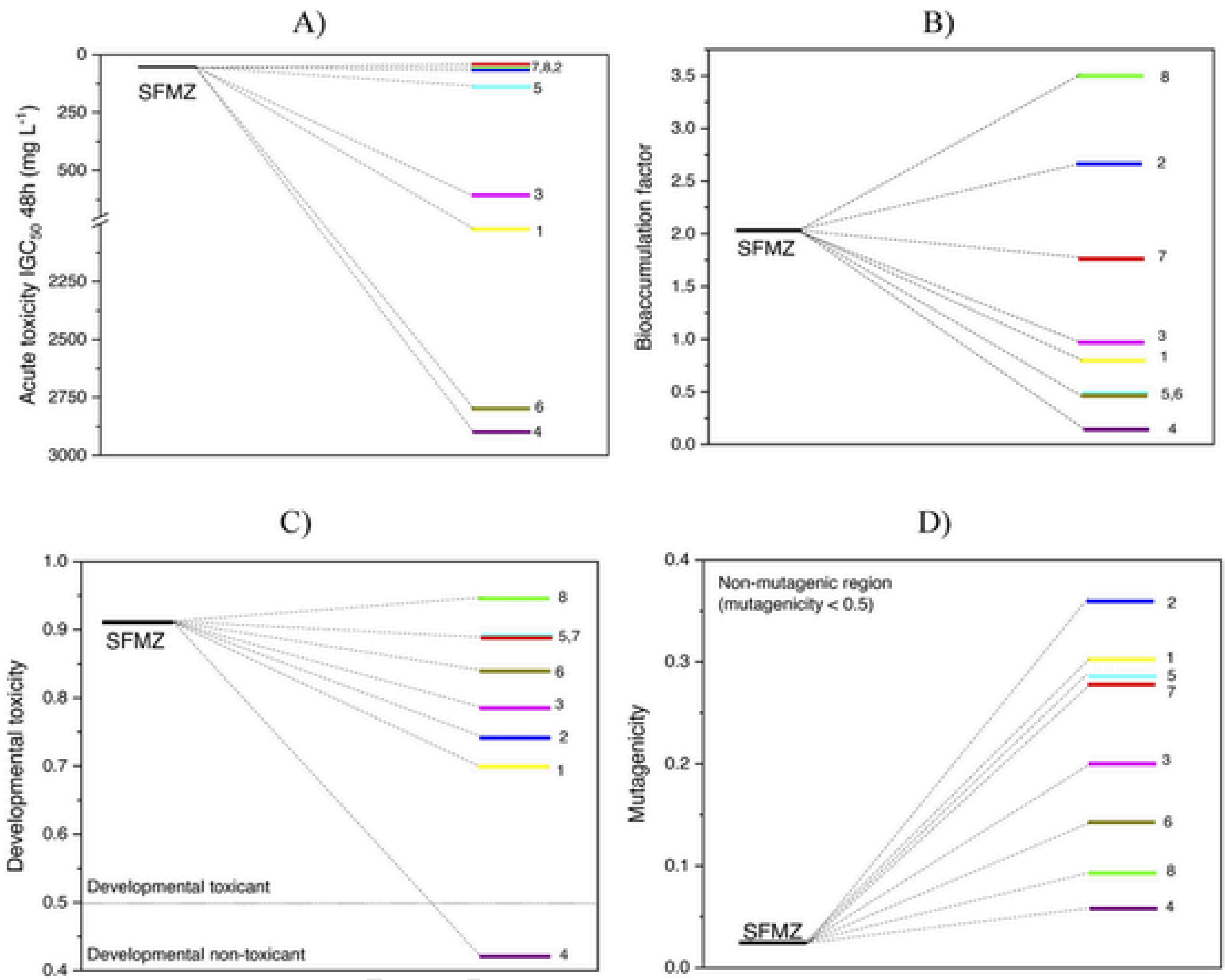

Fig. 14. – A) Acute toxicity of SFMZ and its degradation intermediates on *T. pyriformis* (IGC_{50} 48 h); B) Bioaccumulation factor; C) Developmental toxicity; D) Mutagenicity.

Table 6 –
Comparison of the photocatalytic degradation efficiency of SFMZ in the related literature.

Material	Type of lamp	Cat. dosage	Volume	[SFMZ]	Degradation	Ref
TiO_2-5% $KNbO_3$-0.25% g-C_3N_4	Osram Ultra Vitalux (300 W)	100 mg L^{-1}	0.5 L	10 mg L^{-1}	90% (300 min)	This work
TiO_2/Bi_2O_3/powdered activated carbon	Xenon (300 W)	1000 mg L^{-1}	0.25 L	20 mg L^{-1}	96% (120 min)	[31]
BiOCl/g-C_3N_4	Xenon (300 W)	400 mg L^{-1}	0.1 L	10 mg L^{-1}	80% (80 min)	[86]
g-C_3N_4/activated carbon	Xenon (300 W)	400 mg L^{-1}	0.05 L	20 mg L^{-1}	99% (60 min)	[84]
Carbon xerogel/ZnO	Osram Ultra Vitalux (300 W)	200 mg L^{-1}	0.5 L	10 mg L^{-1}	94% (300 min)	[87]
CeO_2/WO_3	Xenon (200 W)	400 mg L^{-1}	0.1 L	100 mg L^{-1}	100% (180 min)	[85]

Fig. 10 illustrates that the primary active radical responsible for the photodegradation of sulfamerazine during heterogeneous photocatalysis is the hydroxyl radical. This is evident from the significant efficiency loss observed, with removal decreasing from 62% to 10% after 3 h when hydroxyl radical suppression was applied [68]. Furthermore, the suppression of the formation of the superoxide active radical during the experiment also led to a reduced degradation efficiency, suggesting its involvement in the photodegradation mechanism. Drawing upon these observations, the following mechanism is suggested to illustrate the generation of active radicals throughout the photocatalytic processTop of Form (Eqs. 2–7):

$$\text{Photocatalyst} + \lambda \rightarrow e^- + h^+ \quad (2)$$

$$H_2O + h^+ \rightarrow {}^\bullet OH + H^+ \quad (3)$$

$$O_2 + e^- \rightarrow O_2^{\bullet -} \quad (4)$$

$$^\bullet OH + {}^\bullet OH \rightarrow H_2O_2 \quad (5)$$

$$H_2O_2 + e^- \rightarrow {}^\bullet OH + OH^- \quad (6)$$

$$H_2O_2 + O_2^{\bullet-} \rightarrow {}^{\bullet}OH + O_2 + OH^- \tag{7}$$

To better understand the mechanism of active radical generation during the photonic excitation process, the energy levels of both the conduction band (E_{CB}) and valence band (E_{VB}) were estimated for the semiconductors investigated in this study. Eqs. 8 and 9 were employed to conduct this assessment [69]:

$$E_{CB} = \chi - E^e - 0.5E_g \tag{8}$$

$$E_{VB} = E_{CB} + E_g \tag{9}$$

where E^e is the energy of free electrons ($E^e = 4.5$ eV vs hydrogen reference), χ is the absolute electronegativity of each semiconductor ($\chi_{TiO2} = 5.81$ eV, $\chi_{g-C3N4} = 4.73$ eV, and $\chi_{KNbO3} = 5.27$ eV), and E_g is the band-gap energy [70].

The results obtained are shown in Table 4.

Observing the energy potentials of the TiO_2 ($E_{CB} = -0.35$ eV and $E_{VB} = 2.98$ eV), $KNbO_3$ ($E_{CB} = -0.85$ eV and $E_{VB} = 2.40$ eV), and g-C_3N_4 ($E_{CB} = -1.22$ eV and $E_{VB} = 1.68$ eV), the production of hydroxyl radicals through the oxidation of water ($E^0 = 2.73$ eV) can only occur at the valence band of the TiO_2 during heterogeneous photocatalysis, even after the formation of the suggested heterojunctions [71,72]. Given that the hydroxyl radical was determined to be the primary agent responsible for the degradation of sulfamerazine, it is anticipated that the electron holes created during photonic activation will be concentrated in the valence band (VB) of TiO_2 during the degradation process. Consequently, it is probable that the charge transfer in the ternary material is happening through the Z-scheme pathway, considering that this charge transfer mechanism would enable the accumulation of electron holes in the valence band of the TiO_2. Therefore, acknowledging that a Z-scheme charge transfer pathway is stabilized for the $TiO_2/KNbO_3$/g-C_3N_4 heterojunction, Fig. 11 depicts the mechanisms underlying charge transfer and the generation of active radicals in the photocatalytic process for the proposed ternary material.

Fig. 12 shows the results for the chronoamperometry and open-circuit potential (OCP) tests, aiming to further evaluate the charge transfer dynamics of the photocatalysts developed.

The chronoamperometry tests (Fig. 12 A) show that the TiO_2-5% $KNbO_3$-0.25% g-C_3N_4 exhibits the most substantial photocurrent generation among the assessed photocatalysts. This superior result can be linked to the Z-scheme heterojunctions formed between the semiconductors present in the ternary catalyst, which facilitate charge transport during photonic activation and, consequently, enhance the photocatalytic efficiency of the composite catalyst [73,74].

Regarding the OCP plots displayed in Fig. 12B, the change in OCP over time ($dOCP/dt$) when light exposure ceases can be linked to the surface recombination of photogenerated charge carriers, where higher $dOCP/dt$ values suggest a swifter recombination process. The $dOCP/dt$ calculated for the pure TiO_2 is equal to 0.0198 V s^{-1}, whereas the $dOCP/dt$ of the TiO_2-5% $KNbO_3$-0.25% g-C_3N_4 was 0.0095 V s^{-1}, providing further evidence that the ternary composite exhibits reduced recombination rates compared to pure TiO_2. Utilizing data obtained from the OCP experiments, Eq. 10 can be applied to estimate the average lifetime of photogenerated charge carriers [75]:

$$\tau_n = \frac{k_b T}{e}\left(\frac{dOCP}{dt}\right)^{-1} \tag{10}$$

Where τ_n represents the average lifetime of photogenerated charge carriers (s), e denotes the elementary charge of a single electron (1.602×10^{-19} C), k_b equals the Boltzmann constant (1.38×10^{-23} K^{-1}), T is the operating temperature of the experiment (K), and $dOCP/dt$ indicates the slope of the voltage change when light irradiation is ceased.

Using Eq. 10, a τ_n value of 2.67 s was obtained for the TiO_2-5% $KNbO_3$-0.25% g-C_3N_4, showing a noteworthy enhancement in the longevity of charge carriers when contrasted with the TiO_2, which has a τ_n of 1.28 s. The observation that photogenerated charge carriers undergo recombination at a faster rate in pure TiO_2 than in the TiO_2-5% $KNbO_3$-0.25% g-C_3N_4 offers additional support for the beneficial influence of the suggested heterojunctions on the charge transport mechanism during light-induced activation, showing that the recombination process was partially mitigated in the ternary photocatalyst.

LC-ESI-MS/MS was used to elucidate the degradation pathway of the SFMZ during the photocatalytic process (Figure S1). Table 5 summarizes the information on degradation products identified and Fig. 13 shows the proposed degradation pathways.

According to previous studies, hydroxylation of the aniline ring, -S-N- and -C-S- cleavage of the sulfonyl group, and N-C cleavage of the pyrimidine ring are the dominant mechanisms during SFMZ degradation via processes involving the hydroxyl radical [76–79]. In this study, hydroxylation of the aniline ring, together with cleavage of the N-C bond and ring opening of the pyrimidine group, led to the formation of **5** ($C_{10}H_{14}N_4O_4S$, $m/z = 287$) and **7** ($C_{10}H_{15}N_3O_4S$, $m/z = 274$). The loss of the amine group and successive hydroxylation in 7 generated 1 ($C_4H_{10}N_2O_4S$, $m/z = 183$). Oxidation of the amine, giving rise to phenylhydroxylamine and subsequently nitrosobenzene, is the route proposed for the formation of 8 ($C_{11}H_{10}N_4O_3S$, $m/z = 279$). This mechanism has already been described in the literature in studies of the oxidation of aromatic amines by catalytic processes [80].

The attack of hydroxyl radicals promoting hydroxylation of the 4-amino benzenesulfonamide ring, cleavage of the S-N bond, and extrusion of SO_2/Smiles-type rearrangement are proposed for the generation of 3 ($C_{10}H_{13}N_3O_2$, $m/z = 208$). This route and its degradation products have already been described in the literature in studies of oxidative processes [78,81,82]. Demethylation of SFMZ's pyrimidine ring, followed by SO_2 extrusion, also generated degradation product **2** ($C_{10}H_{14}N_4$, $m/z = 191$) [83]. Finally, the oxidation of the methyl group to the carboxyl group, the attack and breaking of the S-N bond, and the opening of the pyrimidine ring generated 6 ($C_5H_7N_3O_2$, $m/z = 142$) [83].

Studies in the literature show that breaking the aromatic rings of intermediate degradation products generally forms carboxylic acids, which are eventually mineralized into CO_2 and H_2O [76–79]. Under the conditions applied in this study, the final SFMZ degradation route generated 2,3-dihydroxybutanedioic acid, identified by number 4 ($C_4H_6O_6$, $m/z = 151$). The proposed formation of this aliphatic acid is related to the successive attack of hydroxyl radicals on the open ring of intermediate 6, resulting in the loss of the amine groups and the oxidation of the final structure.

To assess the biosecurity of the suggested method for SFMZ photodegradation, quantitative structure-activity relationship (QSAR) predictions using the Toxicity Estimation Software Tool (T.E.S.T.) were employed to evaluate the toxicity of SFMZ and its degradation intermediates (1–8) based on various factors: acute toxicity (*T. pyriformis* IGC_{50} 48 h), bioaccumulation potential, developmental toxicity, and mutagenicity [78]. The results obtained are displayed in Fig. 14.

As depicted in Fig. 14 A, SFMZ exhibited an IGC_{50} value of 65.7 mg L^{-1}, designating it as a harmful pollutant ($IGC_{50} <$ 100 mg L^{-1}). However, most of the SFMZ degradation intermediates exhibited elevated IGC_{50} values, classifying them as either harmful or non-harmful ($IGC_{50} >$ 100 mg L^{-1}), with the exceptions being intermediates 7, 8, and 2, which displayed similar IGC_{50} values to the original SFMZ molecule [78]. Consequently, it is expected that the overall acute toxicity of SFMZ was diminished during the degradation process. Fig. 14B illustrates that the process also reduced the bioaccumulation potential of the majority of the intermediates. Furthermore, SFMZ was identified as a "developmental toxicant," but the photodegradation process reduced the toxicity of all degradation intermediates, except for intermediate 8 (Fig. 14 C). Lastly, Fig. 14D demonstrates that the process preserved the mutagenicity status of all intermediates, as each of them was rated "non-mutagenic" by the prediction algorithm (mutagenicity < 0.5). In summary, the proposed photodegradation process not only effectively eliminates SFMZ but also diminishes its overall toxicity; nonetheless, it is crucial to acknowledge that certain products retained some level of toxicity in the aquatic environment. Consequently, during the photocatalytic degradation process, it might be essential to consider extending the treatment duration appropriately to attain complete mineralization.

Finally, Table 6 presents a comparative analysis between the findings of this study and relevant literature regarding the photodegradation of sulfamerazine.

Table 6 illustrates that the related literature on SFMZ photodegradation utilizes a quite diverse array of reactional systems and conditions during the degradation process, often employing smaller reactor volumes and higher doses of photocatalyst, posing challenges for accurate comparison of material efficiency. Nevertheless, given the larger reactor volume and lower catalyst dosage employed in the present study, the results obtained appear to align reasonably well with previously reported findings.

4. Conclusion

The optimized ternary material (TiO_2-5% $KNbO_3$-0.25% g-C_3N_4) demonstrated superior photocatalytic performance compared to all other materials evaluated in the proposed degradation tests. In this context, the TiO_2-5% $KNbO_3$-0.25% g-C_3N_4 achieved close to 90% degradation of the sulfamerazine in 5 h under simulated sunlight, with 55% TOC removal; as a comparison, the pure TiO_2 achieved approximately 50% degradation in the same period. The formation of heterojunctions between titanium oxide, potassium niobate, and carbon nitride played a pivotal role in enhancing the photocatalytic efficiency of this material, due to their effect on the suppression of charge recombination during the photodegradation process through the formation of Z-scheme heterojunctions, as demonstrated by the OCP tests and chronoamperometry tests. Furthermore, the modifications proposed also led to beneficial structural, optical, and morphological modifications, such as the enlargement of both the specific surface area and visible light absorption capacity of the ternary composite. The photocatalytic mechanism was predominantly influenced by the generation of hydroxyl radicals, further indicating the formation of a Z-scheme charge transfer pathway between the semiconductors during photonic excitation. Furthermore, the proposed degradation pathway determined by LC-ESI-MS/MS indicated a decrease in the toxicity of SFMZ due to the formation of mostly less toxic intermediates.

CRediT authorship contribution statement

Tiago Campos: Visualization, Validation, Software, Resources, Methodology, Investigation, Formal analysis. **Gilmar Thim:** Visualization, Validation, Supervision, Software, Resources, Methodology, Investigation, Funding acquisition, Formal analysis. **Yu Lianqing:** Validation, Supervision, Software, Resources, Methodology, Investigation, Formal analysis. **Robson Rocha:** Visualization, Validation, Software, Resources, Methodology, Investigation, Funding acquisition, Formal analysis. **Renata Colombo:** Writing – review & editing, Writing – original draft, Visualization, Validation, Software, Resources, Methodology, Investigation, Funding acquisition, Formal analysis. **Liana Rodrigues:** Writing – review & editing, Writing – original draft, Visualization, Validation, Supervision, Software, Resources, Project administration, Methodology, Investigation, Funding acquisition, Formal analysis, Conceptualization. **Marcos Lanza:** Writing – review & editing, Writing – original draft, Visualization, Validation, Supervision, Software, Resources, Project administration, Methodology, Investigation, Funding acquisition, Formal analysis, Conceptualization. **Nicolas De Moraes:** Writing – review & editing, Writing – original draft, Visualization, Validation, Software, Resources, Methodology, Investigation, Formal analysis, Conceptualization.

Declaration of Competing Interest

The authors declare that they have no known competing financial interests or personal relationships that could have appeared to influence the work reported in this paper.

Acknowledgments

The authors are grateful to the São Paulo Research Foundation - FAPESP (Grants #2014/50945–4, #2017/10118–0, and #2022/04058–2) and National Council for Scientific and Technological Development – CNPq (Grants #465571/2014–0 and #303943/2021–1) for the financial assistance provided in support of this work.

Data Availability

Data will be made available on request.

Appendix A. Supporting information

Supplementary data associated with this article can be found in the online version at doi:10.1016/j.jece.2024.113026.

References

[1] J. Wang, R. Zhuan, Degradation of antibiotics by advanced oxidation processes: an overview, Sci. Total Environ. 701 (2020) 135023, https://doi.org/10.1016/J.SCITOTENV.2019.135023.
[2] I.M. Al-Riyami, M. Ahmed, A. Al-Busaidi, B.S. Choudri, Antibiotics in wastewaters: a review with focus on Oman, Appl. Water Sci. 8 (2018), https://doi.org/10.1007/s13201-018-0846-z.
[3] S. Deylami, M.H. Sabzevari, M. Ghaedi, M.H.A. Azqhandi, F. Marahel, Efficient photodegradation of disulfine blue dye and Tetracycline over Robust and Green g-CN/Ag3VO4/PAN nanofibers: Experimental design, RSM, RBF-NN and ANFIS modeling, Process Saf. Environ. Prot. 169 (2023) 71–81, https://doi.org/10.1016/j.psep.2022.10.080.
[4] M. Frieri, K. Kumar, A. Boutin, Antibiotic resistance, J. Infect. Public Health 10 (2017) 369–378, https://doi.org/10.1016/j.jiph.2016.08.007.
[5] A.P.S. Batista, F.C.C. Pires, A.C.S.C. Teixeira, Photochemical degradation of sulfadiazine, sulfamerazine and sulfamethazine: Relevance of concentration and heterocyclic aromatic groups to degradation kinetics, J. Photochem. Photobiol. A Chem. 286 (2014) 40–46, https://doi.org/10.1016/j.jphotochem.2014.04.022.
[6] L.A. Poirier, D.R. Doerge, D.W. Gaylor, M.A. Miller, R.J. Lorentzen, D.A. Casciano, F.F. Kadlubar, B.A. Schweiz, An FDA review of sulfamethazine toxicity, Regul. Toxicol. Pharmacol. 30 (1999) 217–222, https://doi.org/10.1006/rtph.1999.1348.
[7] A. Fabiańska, A. Białk-Bielińska, P. Stepnowski, S. Stolte, E.M. Siedlecka, Electrochemical degradation of sulfonamides at BDD electrode: Kinetics, reaction pathway and eco-toxicity evaluation, J. Hazard. Mater. 280 (2014) 579–587, https://doi.org/10.1016/J.JHAZMAT.2014.08.050.
[8] M. Beshtar, A.A. Asgharinezhad, A. Larimi, Ultra-deep photocatalytic oxidative desulfurization of liquid fuels by Ti@CeO2/ZnO nanophotocatalyst under visible light and mild operating conditions, J. Ind. Eng. Chem. (2024) 1–13, https://doi.org/10.1016/j.jiec.2024.01.017.
[9] O. Hosseini, V. Zare-Shahabadi, M. Ghaedi, M.H.A. Azqhandi, Experimental design, RSM and ANN modeling of tetracycline photocatalytic degradation using LDH@CN, J. Environ. Chem. Eng. 10 (2022) 108345, https://doi.org/10.1016/j.jece.2022.108345.
[10] S. Wang, J.H. Yun, B. Luo, T. Butburee, P. Peerakiatkhajohn, S. Thaweesak, M. Xiao, L. Wang, Recent progress on visible light responsive heterojunctions for photocatalytic applications, J. Mater. Sci. Technol. 33 (2017) 1–22, https://doi.org/10.1016/j.jmst.2016.11.017.
[11] Z. Chen, T. Ma, Z. Li, W. Zhu, L. Li, Enhanced photocatalytic performance of S-scheme CdMoO4/CdO nanosphere photocatalyst, J. Mater. Sci. Technol. 179 (2024) 198–207, https://doi.org/10.1016/j.jmst.2023.07.029.
[12] Y. Zheng, Y. Liu, X. Guo, Z. Chen, W. Zhang, Y. Wang, X. Tang, Y. Zhang, Y. Zhao, Sulfur-doped g-C3N4/rGO porous nanosheets for highly efficient photocatalytic degradation of refractory contaminants, J. Mater. Sci. Technol. 41 (2020) 117–126, https://doi.org/10.1016/J.JMST.2019.09.018.
[13] F.J. Beltrán, A. Rey, Solar or UVA-visible photocatalytic ozonation of water contaminants, Molecules 22 (2017), https://doi.org/10.3390/molecules22071177.
[14] H. Wang, L. Zhang, Z. Chen, J. Hu, S. Li, Z. Wang, J. Liu, X. Wang, Semiconductor heterojunction photocatalysts: design, construction, and photocatalytic

performances, Chem. Soc. Rev. 43 (2014) 5234–5244, https://doi.org/10.1039/c4cs00126e.

[15] W. Zhu, L. Yang, F. Liu, Z. Si, M. Huo, Z. Li, Z. Chen, Metal Ni nanoparticles in-situ anchored on CdS nanowires as effective cocatalyst for boosting the photocatalytic H2 production and degradation activity, J. Alloy. Compd. 973 (2024) 172747, https://doi.org/10.1016/j.jallcom.2023.172747.

[16] J. Low, J. Yu, M. Jaroniec, S. Wageh, A.A. Al-Ghamdi, Heterojunction Photocatalysts, Adv. Mater. 29 (2017), https://doi.org/10.1002/adma.201601694.

[17] B.H. Park, H. Park, T. Kim, S.J. Yoon, Y. Kim, N. Son, M. Kang, S-scheme assisted Cu2O/ZnO flower-shaped heterojunction catalyst for breakthrough hydrogen evolution by water splitting, Int. J. Hydrog. Energy 46 (2021) 38319–38335, https://doi.org/10.1016/j.ijhydene.2021.09.087.

[18] H. Ge, F. Xu, B. Cheng, J. Yu, W. Ho, S-Scheme Heterojunction TiO2/CdS Nanocomposite Nanofiber as H2-Production Photocatalyst, ChemCatChem 11 (2019) 6301–6309, https://doi.org/10.1002/cctc.201901486.

[19] H. Yu, M. Zhao, C. Xue, J. Huang, N. Zhao, L. Kong, All-solid-state Z-scheme nanojunction PW12/Ag/ZnO photocatalyst: Effective carriers transfer promotion and enhanced visible light driven, J. Mol. Struct. 1300 (2024) 137272, https://doi.org/10.1016/j.molstruc.2023.137272.

[20] Y. Li, H. Chen, L. Wang, T. Wu, Y. Wu, Y. He, KNbO3/ZnO heterojunction harvesting ultrasonic mechanical energy and solar energy to efficiently degrade methyl orange, Ultrason. Sonochem. 78 (2021), https://doi.org/10.1016/j.ultsonch.2021.105754.

[21] E. Boorboor Azimi, A. Badiei, M. Hossaini Sadr, Dramatic visible photocatalytic performance of g-C3N4-based nanocomposite due to the synergistic effect of AgBr and ZnO semiconductors, J. Phys. Chem. Solids (2018), https://doi.org/10.1016/j.jpcs.2018.06.024.

[22] N. Kumaresan, M.M.A. Sinthiya, M. Praveen Kumar, S. Ravichandran, R. Ramesh Babu, K. Sethurman, K. Ramamurthi, Investigation on the g-C3N4 encapsulated ZnO nanorods heterojunction coupled with GO for effective photocatalytic activity under visible light irradiation, Arab. J. Chem. 13 (2020) 2826–2843, https://doi.org/10.1016/j.arabjc.2018.07.013.

[23] C.H. Wang, D.D. Qin, D.L. Shan, J. Gu, Y. Yan, J. Chen, Q.H. Wang, C.H. He, Y. Li, J.J. Quan, X.Q. Lu, Assembly of g-C3N4-based type II and Z-scheme heterojunction anodes with improved charge separation for photoelectrojunction water oxidation, Phys. Chem. Chem. Phys. 19 (2017) 4507–4515, https://doi.org/10.1039/c6cp08066a.

[24] N.P. de Moraes, R. Souto, T.M.B. Campos, G.P. Thim, Y. Lianqing, R.S. Rocha, L.A. Rodrigues, M.Roberto de, Vasconcelos Lanza, Using KNbO3 catalyst produced from a simple solid-state synthesis method in a new piezophotocatalytic ozonation hybrid process, Ceram. Int. (2023), https://doi.org/10.1016/j.ceramint.2023.06.265.

[25] J.G.M. de Sousa, T.V.C. da Silva, N.P. de Moraes, M.L. Caetano Pinto da Silva, R. da Silva Rocha, R. Landers, L.A. Rodrigues, Visible light-driven ZnO/g-C3N4/carbon xerogel ternary photocatalyst with enhanced activity for 4-chlorophenol degradation, Mater. Chem. Phys. 256 (2020) 123651, https://doi.org/10.1016/j.matchemphys.2020.123651.

[26] N.P. de Moraes, M.L.C.P. da Silva, T.M.B. Campos, G.P. Thim, L.A. Rodrigues, Novel synthetic route for low-cost carbon-modified TiO2 with enhanced visible light photocatalytic activity: carbon content and calcination effects, J. Sol. -Gel Sci. Technol. 87 (2018) 380–390, https://doi.org/10.1007/s10971-018-4700-4.

[27] V. de J. Gaffney, V.V. Cardoso, M.J. Benoliel, C.M.M. Almeida, Chlorination and oxidation of sulfonamides by free chlorine: Identification and behaviour of reaction products by UPLC-MS/MS, J. Environ. Manag. 166 (2016) 466–477, https://doi.org/10.1016/j.jenvman.2015.10.048.

[28] S. Parambadath, A. Mathew, M.J. Barnabas, K.M. Rao, C.S. Ha, Periodic mesoporous organosilica (PMO) containing bridged succinamic acid groups as a nanocarrier for sulfamerazine, sulfadiazine and famotidine: adsorption and release study, Microporous Mesoporous Mater. 225 (2016) 174–184, https://doi.org/10.1016/j.micromeso.2015.12.016.

[29] X. Liu, F. Huang, Y. Yu, Y. Jiang, K. Zhao, Y. He, Y. Xu, Y. Zhang, Determination and toxicity evaluation of the generated byproducts from sulfamethazine degradation during catalytic oxidation process, Chemosphere 226 (2019) 103–109, https://doi.org/10.1016/j.chemosphere.2019.03.125.

[30] K. Zhang, Z. Luo, T. Zhang, N. Gao, Y. Ma, Degradation effect of sulfa antibiotics by potassium ferrate combined with ultrasound (Fe(VI)-US), Biomed. Res. Int. 2015 (2015), https://doi.org/10.1155/2015/169215.

[31] X. Zhuang, X. Li, Y. Yang, N. Wang, Y. Shang, Z. Zhou, J. Li, H. Wang, Enhanced sulfamerazine removal via adsorption-photocatalysis using Bi2O3-TiO2/PAC ternary nanoparticles, Water (Switz.) 12 (2020), https://doi.org/10.3390/w12082273.

[32] N.P. de Moraes, R.B. Valim, R. da Silva Rocha, M.L.C.P. da Silva, T.M.B. Campos, G.P. Thim, L.A. Rodrigues, Effect of synthesis medium on structural and photocatalytic properties of ZnO/carbon xerogel composites for solar and visible light degradation of 4-chlorophenol and bisphenol A, Colloids Surf. A Physicochem. Eng. Asp. 584 (2020) 124034, https://doi.org/10.1016/j.colsurfa.2019.124034.

[33] F. Fina, S.K. Callear, G.M. Carins, J.T.S. Irvine, Structural investigation of graphitic carbon nitride via XRD and neutron diffraction, Chem. Mater. 27 (2015) 2612–2618, https://doi.org/10.1021/acs.chemmater.5b00411.

[34] S. Ghodsi, A. Esrafili, R.R. Kalantary, M. Gholami, H.R. Sobhi, Synthesis and evaluation of the performance of g-C3N4/Fe3O4/Ag photocatalyst for the efficient removal of diazinon: Kinetic studies, J. Photochem. Photobiol. A Chem. 389 (2020) 112279, https://doi.org/10.1016/j.jphotochem.2019.112279.

[35] H. Azizi-Toupkanloo, M. Karimi-Nazarabad, M. Shakeri, M. Eftekhari, Photocatalytic mineralization of hard-degradable morphine by visible light-driven Ag@g-C3N4 nanostructures, Environ. Sci. Pollut. Res. 26 (2019) 30941–30953, https://doi.org/10.1007/s11356-019-06274-9.

[36] R. Grazziotin-Soares, M.H. Nekoofar, T. Davies, R. Hübler, N. Meraji, P.M.H. Dummer, Crystalline phases involved in the hydration of calcium silicate-based cements: semi-quantitative Rietveld X-ray diffraction analysis, Aust. Endod. J. 45 (2019) 26–32 https://doi.org/10.1111/aej.12226.

[37] J.G.M. de Sousa, T.V.C. da Silva, N.P. de Moraes, M.L. Caetano Pinto da Silva, R. da Silva Rocha, R. Landers, L.A. Rodrigues, Visible light-driven ZnO/g-C3N4/carbon xerogel ternary photocatalyst with enhanced activity for 4-chlorophenol degradation, Mater. Chem. Phys. 256 (2020) 123651, https://doi.org/10.1016/j.matchemphys.2020.123651.

[38] H. Gao, J. Liu, J. Zhang, Z. Zhu, G. Zhang, Q. Liu, Influence of carbon and yttrium co-doping on the photocatalytic activity of mixed phase TiO2, Cuihua Xuebao/, Chin. J. Catal. 38 (2017) 1688–1696, https://doi.org/10.1016/S1872-2067(17)62893-6.

[39] S. Varnagiris, A. Medvids, M. Lelis, D. Milcius, A. Antuzevics, Black carbon-doped TiO2 films: Synthesis, characterization and photocatalysis, J. Photochem. Photobiol. A Chem. 382 (2019) 111941, https://doi.org/10.1016/j.jphotochem.2019.111941.

[40] K. Rajkumari, D. Das, G. Pathak, L. Rokhum, Waste-to-useful: A biowaste-derived heterogeneous catalyst for a green and sustainable Henry reaction, N. J. Chem. 43 (2019) 2134–2140, https://doi.org/10.1039/c8nj05029e.

[41] S. Jain, J. Shah, N.S. Negi, C. Sharma, R.K. Kotnala, Significance of interface barrier at electrode of hematite hydroelectric cell for generating ecopower by water splitting, Int. J. Energy Res. 43 (2019) 4743–4755, https://doi.org/10.1002/ER.4613.

[42] F.M. Chang, S. Brahma, J.H. Huang, Z.Z. Wu, K.Y. Lo, Strong correlation between optical properties and mechanism in deficiency of normalized self-assembly ZnO nanorods, Sci. Rep. 9 (2019) 1–9, https://doi.org/10.1038/s41598-018-37601-8.

[43] V. Alman, K. Singh, T. Bhat, A. Sheikh, S. Gokhale, Sunlight Assisted improved photocatalytic degradation of rhodamine B using Pd-loaded g-C3N4/WO3 nanocomposite, Appl. Phys. A Mater. Sci. Process. 126 (2020) 1–9, https://doi.org/10.1007/s00339-020-03914-7.

[44] P.A. Connor, K.D. Dobson, A. James, McQuillan, Infrared spectroscopy of the TiO2/aqueous solution interface, Langmuir 15 (1999) 2402–2408 https://doi.org/10.1021/LA980855D/ASSET/IMAGES/LARGE/LA980855DF00006.JPEG.

[45] J. Yu, Z. Chen, Y. Wang, Y. Ma, Z. Feng, H. Lin, Y. Wu, L. Zhao, Y. He, Synthesis of KNbO3/g-C3N4 composite and its new application in photocatalytic H2 generation under visible light irradiation, J. Mater. Sci. 53 (2018) 7453–7465, https://doi.org/10.1007/s10853-018-2119-5.

[46] T. Narkbuakaew, P. Sujaridworakun, Synthesis of Tri-S-Triazine Based g-C3N4 Photocatalyst for Cationic Rhodamine B Degradation under Visible Light, Top. Catal. 63 (2020) 1086–1096 https://doi.org/10.1007/S11244-020-01375-Z/FIGURES/11.

[47] N. Mojoudi, N. Mirghaffari, M. Soleimani, H. Shariatmadari, C. Belver, J. Bedia, Phenol adsorption on high microporous activated carbons prepared from oily sludge: equilibrium, kinetic and thermodynamic studies, Sci. Rep. 9 (2019) 1–12, https://doi.org/10.1038/s41598-019-55794-4.

[48] M. Beshtar, F. Khorasheh, A. Larimi, A. Akbar Asgharinezhad, Photocatalytic oxidative desulfurization of model fuel using iron-molybdenum nanocatalyst based on cerium oxide (FeyMox/CeO2) under visible light, Fuel 360 (2024) 130549, https://doi.org/10.1016/j.fuel.2023.130549.

[49] I.S. Golovina, V.P. Bryksa, V.V. Strelchuk, I.N. Geifman, A.A. Andriiko, Size effects in the temperatures of phase transitions in KNbO3 nanopowder, J. Appl. Phys. 113 (2013), https://doi.org/10.1063/1.4801794.

[50] D. Chen, L. Zou, S. Li, F. Zheng, Nanospherical like reduced graphene oxide decorated TiO2 nanoparticles: An advanced catalyst for the hydrogen evolution reaction, Sci. Rep. 6 (2016) 1–8, https://doi.org/10.1038/srep20335.

[51] G.K.L. Goh, F.F. Lange, S.M. Haile, C.G. Levi, Hydrothermal synthesis of KNbO3 and NaNbO3 powders, J. Mater. Res. 18 (2003) 338–345, https://doi.org/10.1557/JMR.2003.0044.

[52] D.T. Trung, J.G. Fisher, Controlled-Atmosphere Sintering of KNbO3, Appl. Sci. 2020, Vol. 10, Page 2131. 10 (2020) 2131. https://doi.org/10.3390/APP10062131.

[53] N. Chaiyo, A. Ruangphanit, R. Muanghlua, S. Niemcharoen, B. Boonchom, N. Vittayakorn, Synthesis of potassium niobate (KNbO3) nano-powder by a modified solid-state reaction, J. Mater. Sci. 46 (2011) 1585–1590, https://doi.org/10.1007/s10853-010-4967-5.

[54] A. Magrez, E. Vasco, J.W. Seo, C. Dicker, N. Setter, L. Forró, Growth of single-crystalline KNbO3 nanostructures, J. Phys. Chem. B. 110 (2006) 58–61, https://doi.org/10.1021/jp053800a.

[55] A. Chowdhury, S. O'Callaghan, T.A. Skidmore, C. James, S.J. Milne, Nanopowders of Na0.5K0.5NbO3 Prepared by the Pechini Method, J. Am. Ceram. Soc. 92 (2009) 758–761, https://doi.org/10.1111/J.1551-2916.2009.02950.X.

[56] P. Yang, J. Wang, G. Yue, R. Yang, P. Zhao, L. Yang, X. Zhao, D. Astruc, Constructing mesoporous g-C3N4/ZnO nanosheets catalyst for enhanced visible-light driven photocatalytic activity, J. Photochem. Photobiol. A Chem. 388 (2020) 112169, https://doi.org/10.1016/j.jphotochem.2019.112169.

[57] N.P. de Moraes, L.A. Bacetto, G.S. dos Santos, M.L.C. Pinto da Silva, J.P.B. Machado, T.M.B. Campos, G.P. Thim, L.A. Rodrigues, Synthesis of novel ZnO/carbon xerogel composites: effect of carbon content and calcination temperature on their structural and photocatalytic properties, Ceram. Int. 45 (2019) 3657–3667, https://doi.org/10.1016/j.ceramint.2018.11.027.

[58] S. Salehian, A. Larimi, A.A. Asgharinezhad, N. Khallaghi, T.N. Borhani, C. Ghotbi, Magnetic Z-scheme bismuth molybdate(1-x)/Fe3O4@MIL-125(Ti)(x) nanocomposite as a high-performance visible-light-active photocatalyst for ultra-deep oxidative desulfurization of liquid fuel, Surf. Interfaces 42 (2023) 103432,

https://doi.org/10.1016/j.surfin.2023.103432.
[59] N.P. de Moraes, F.A. Torezin, G.V. Jucá Dantas, J.G.M. de Sousa, R.B. Valim, R. da Silva Rocha, R. Landers, M.L.C.P. da Silva, L.A. Rodrigues, TiO2/Nb2O5/carbon xerogel ternary photocatalyst for efficient degradation of 4-chlorophenol under solar light irradiation, Ceram. Int. 46 (2020) 14505–14515, https://doi.org/10.1016/j.ceramint.2020.02.249.
[60] N.P. de Moraes, R.B. Anselmo, L.O. Sartor, G.V.J. Dantas, L.A. Rodrigues, L. Chaguri e Carvalho, Spray drying as feasible processing technique to enhance the photocatalytic activity of the Nb2O5/carbon xerogel composite, Mater. Lett. 273 (2020) 127932, https://doi.org/10.1016/j.matlet.2020.127932.
[61] P. Makuła, M. Pacia, W. Macyk, How To Correctly Determine the Band Gap Energy of Modified Semiconductor Photocatalysts Based on UV-Vis Spectra, J. Phys. Chem. Lett. 9 (2018) 6814–6817, https://doi.org/10.1021/acs.jpclett.8b02892.
[62] B. Modak, S.K. Ghosh, Improving KNbO3 photocatalytic activity under visible light, RSC Adv. 6 (2016) 9958–9966, https://doi.org/10.1039/c5ra26079e.
[63] N.P. de Moraes, L.A. Bacetto, G.S. dos Santos, M.L.C. Pinto da Silva, J.P.B. Machado, T.M.B. Campos, G.P. Thim, L.A. Rodrigues, Synthesis of novel ZnO/carbon xerogel composites: Effect of carbon content and calcination temperature on their structural and photocatalytic properties, Ceram. Int. 45 (2019) 3657–3667, https://doi.org/10.1016/j.ceramint.2018.11.027.
[64] N.P. de Moraes, R.D.M. dos Santos, M.E.V. Gouvêa, A. de Siervo, R. da Silva Rocha, D.A. Reddy, Y. Lianqing, M.R. de Vasconcelos Lanza, L.A. Rodrigues, Solar-based photocatalytic ozonation employing novel S-scheme ZnO/Cu2O/CuO/carbon xerogel photocatalyst: effect of pH, salinity, turbidity, and temperature on salicylic acid degradation, Environ. Sci. Pollut. Res. 30 (2023) 98211–98230, https://doi.org/10.1007/s11356-023-29399-4.
[65] Z. Vaez, V. Javanbakht, Synthesis, characterization and photocatalytic activity of ZSM-5/ZnO nanocomposite modified by Ag nanoparticles for methyl orange degradation, J. Photochem. Photobiol. A Chem. 388 (2020) 112064, https://doi.org/10.1016/j.jphotochem.2019.112064.
[66] N.P. de Moraes, A. de Siervo, T.O. Silva, R. da Silva Rocha, D.A. Reddy, Y. Lianqing, M.R. de Vasconcelos Lanza, L.A. Rodrigues, Kraft lignin-based carbon xerogel/zinc oxide composite for 4-chlorophenol solar-light photocatalytic degradation: effect of pH, salinity, and simultaneous Cr(VI) reduction, Environ. Sci. Pollut. Res. (2022), https://doi.org/10.1007/s11356-022-22825-z.
[67] C.C. Yang, C.L. Huang, T.C. Cheng, H.T. Lai, Inhibitory effect of salinity on the photocatalytic degradation of three sulfonamide antibiotics, Int. Biodeterior. Biodegrad. 102 (2015) 116–125, https://doi.org/10.1016/j.ibiod.2015.01.015.
[68] C. Wang, P. Shi, C. Guo, R. Guo, J. Qiu, CuCo2O4/CF cathode with bifunctional and dual reaction centers exhibits high RhB degradation in electro-Fenton systems, J. Electroanal. Chem. 956 (2024) 118072, https://doi.org/10.1016/j.jelechem.2024.118072.
[69] M. Basu, N. Garg, A.K. Ganguli, A type-II semiconductor (ZnO/CuS heterostructure) for visible light photocatalysis, J. Mater. Chem. A. (2014), https://doi.org/10.1039/c3ta15446g.
[70] J. Yan, G. Wu, N. Guan, L. Li, Nb2O5/TiO2 heterojunctions: Synthesis strategy and photocatalytic activity, Appl. Catal. B Environ. 152–153 (2014) 280–288, https://doi.org/10.1016/j.apcatb.2014.01.049.
[71] B.G. Kwon, J. Yoon, Superoxide, anion Radic.: Princ. Appl., J. Korean Ind. Eng. Chem. 20 (2009) 593–602.
[72] M.E. Aguirre, R. Zhou, A.J. Eugene, M.I. Guzman, M.A. Grela, Cu2O/TiO2 heterostructures for CO2 reduction through a direct Z-scheme: Protecting Cu2O from photocorrosion, Appl. Catal. B Environ. 217 (2017) 485–493, https://doi.org/10.1016/j.apcatb.2017.05.058.
[73] P. She, S. Yin, Q. He, X. Zhang, K. Xu, Y. Shang, X. Men, S. Zeng, H. Sun, Z. Liu, A self-standing macroporous Au/ZnO/reduced graphene oxide foam for recyclable photocatalysis and photocurrent generation, Electrochim. Acta 246 (2017) 35–42, https://doi.org/10.1016/j.electacta.2017.06.027.
[74] J. Lee, Z. Li, L. Zhu, S. Xie, X. Cui, Ti3+ self-doped TiO2 via facile catalytic reduction over Al(acac)3 with enhanced photoelectrochemical and photocatalytic activities, Appl. Catal. B Environ. 224 (2018) 715–724, https://doi.org/10.1016/j.apcatb.2017.10.057.
[75] X. Yue, S. Yi, R. Wang, Z. Zhang, S. Qiu, Well-controlled SrTiO3@Mo2C core-shell nanofiber photocatalyst: boosted photo-generated charge carriers transportation and enhanced catalytic performance for water reduction, Nano Energy 47 (2018) 463–473, https://doi.org/10.1016/j.nanoen.2018.03.014.
[76] F. Deng, S. Li, M. Zhou, Y. Zhu, S. Qiu, K. Li, F. Ma, J. Jiang, A biochar modified nickel-foam cathode with iron-foam catalyst in electro-Fenton for sulfamerazine degradation, Appl. Catal. B Environ. 256 (2019) 117796, https://doi.org/10.1016/j.apcatb.2019.117796.
[77] J. Wang, Z. Shu, Z. Chen, J. Su, C. Liu, Iodide ions enhancing sulfamerazine degradation by horseradish peroxidase/H2O2: Degradation products, degradation mechanism and toxicity assessment, J. Clean. Prod. 337 (2022) 130489, https://doi.org/10.1016/j.jclepro.2022.130489.
[78] J. qi Li, Z. wei Zhou, X. Li, Y. ling Yang, J. feng Gao, R. Yu, H. ping Wang, N. Wang, Synergistically boosting sulfamerazine degradation via activation of peroxydisulfate by photocatalysis of Bi2O3-TiO2/PAC under visible light irradiation, Chem. Eng. J. 428 (2022) 132613, https://doi.org/10.1016/j.cej.2021.132613.
[79] M. Yao, M. Xie, S. Zhang, J. Yuan, L. Zhao, R.S. Zhao, Co nanoparticles encapsulated in nitrogen-doped nanocarbon derived from cobalt-modified covalent organic framework as peroxymonosulfate activator for sulfamerazine degradation, Sep. Purif. Technol. 302 (2022) 122145, https://doi.org/10.1016/j.seppur.2022.122145.
[80] B. Singh, D. Mandelli, P.P. Pescarmona, Efficient and selective oxidation of aromatic amines to azoxy derivatives over aluminium and gallium oxide catalysts with nanorod morphology, ChemCatChem 12 (2020) 593–601, https://doi.org/10.1002/cctc.201901378.
[81] L. Zheng, H. Jin, M. Yu, Q. Zhongwei, L. Zhang, C. Shikun, Z. Li, Degradation of sulfamethoxazole by electrochemically activated persulfate using iron anode, Int. J. Chem. React. Eng. 17 (2019) 1–14, https://doi.org/10.1515/ijcre-2018-0160.
[82] K. Kokoszka, J. Wilk, E. Felis, S. Bajkacz, Application of UHPLC-MS/MS method to study occurrence and fate of sulfonamide antibiotics and their transformation products in surface water in highly urbanized areas, Chemosphere 283 (2021) 131189, https://doi.org/10.1016/j.chemosphere.2021.131189.
[83] X. Hu, J. Bao, D. Chen, S. Jalil Shah, S. Subhan, W. Gong, W. Li, X. Luan, Z. Zhao, Z. Zhao, Accelerating the Fe(III)/Fe(II) cycle via enhanced electronic effect in NH2-MIL-88B(Fe)/TPB-DMTP-COF composite for boosting photo-Fenton degradation of sulfamerazine, J. Colloid Interface Sci. 624 (2022) 121–136, https://doi.org/10.1016/j.jcis.2022.05.142.
[84] S. Lu, F. Liu, P. Qiu, M. Qiao, Y. Li, Z. Cheng, N. Xue, X. Hou, C. Xu, Y. Xiang, F. Peng, Z. Guo, Photothermal-assisted photocatalytic degradation with ultrahigh solar utilization: towards practical application, Chem. Eng. J. 379 (2020) 122382, https://doi.org/10.1016/j.cej.2019.122382.
[85] A. Bahadoran, S. Ramakrishna, S. Masudy-Panah, J. Roshan De Lile, B. Sadeghi, J. Li, J.J. Gu, Q. Liu, Novel S-scheme WO3/CeO2 heterojunction with enhanced photocatalytic degradation of sulfamerazine under visible light irradiation, Appl. Surf. Sci. 568 (2021) 150957, https://doi.org/10.1016/j.apsusc.2021.150957.
[86] C. Yang, Q. Rong, F. Shi, M. Cao, G. Li, Y. Xin, W. Zhang, G. Zhang, Rationally designed S-scheme heterojunction of BiOCl/g-C3N4 for photodegradation of sulfamerazine: mechanism insights, degradation pathways and DFT calculation, Chin. Chem. Lett. (2024) 109767, https://doi.org/10.1016/j.cclet.2024.109767.
[87] N.P. de Moraes, R. da Silva Rocha, A. de Siervo, C.C.A. do Prado, T.C.B. de Paiva, T.M.B. Campos, G.P. Thim, M.R. de Vasconcelos Lanza, L.A. Rodrigues, Resorcinol-based carbon xerogel/ZnO composite for solar-light-induced photodegradation of sulfamerazine, Opt. Mater. (Amst.). 128 (2022), https://doi.org/10.1016/j.optmat.2022.112470.